

X-ray bright active galactic nuclei in massive galaxy clusters III: New insights into the triggering mechanisms of cluster AGN

S. Ehlert,^{1,2,3,4*} S.W. Allen,^{1,2,3} W.N. Brandt,^{6,7} R.E.A. Canning,^{1,2,3}
 B. Luo,^{6,7} A. Mantz,^{9,10} R.G. Morris,^{1,2,3} A. von der Linden,^{1,3,5} and Y.Q. Xue,⁸

¹Kavli Institute for Astrophysics and Space Research, Massachusetts Institute of Technology, 77 Massachusetts Ave., Cambridge, MA 02139, USA

²SLAC National Accelerator Laboratory, 2575 Sand Hill Road, Menlo Park, CA 94025, USA

³Department of Physics, Stanford University, 382 Via Pueblo Mall, Stanford, CA 94305-4060, USA

⁴Kavli Institute for Particle Astrophysics and Cosmology, 452 Lomita Mall, Stanford, CA 94305-4085, USA

⁵Dark Cosmology Centre, Niels Bohr Institute, University of Copenhagen, Juliane Maries Vej 30, 2100 Copenhagen, Denmark

⁶Department of Astronomy and Astrophysics, Pennsylvania State University, University Park, PA 16802, USA

⁷Institute for Gravitation and the Cosmos, Department of Physics, Pennsylvania State University, University Park, PA 16802, USA

⁸Key Laboratory for Research in Galaxies and Cosmology, Department of Astronomy, University of Science and Technology of China, Chinese Academy of Sciences, Hefei, Anhui 230026, China

⁹Kavli Institute for Cosmological Physics, 5640 S. Ellis Avenue, Chicago, IL 60637, USA

¹⁰Department of Astronomy and Astrophysics, University of Chicago, 5640 S. Ellis Avenue, Chicago, IL 60637, USA

February 20, 2018

ABSTRACT

We present the results of a new analysis of the X-ray selected Active Galactic Nuclei (AGN) population in the vicinity of 135 of the most massive galaxy clusters in the redshift range of $0.2 < z < 0.9$ observed with *Chandra*. With a sample of more than 11,000 X-ray point sources, we are able to measure, for the first time, evidence for evolution in the cluster AGN population beyond the expected evolution of field AGN. Our analysis shows that overall number density of cluster AGN scales with the cluster mass as $\sim M_{500}^{-1.2}$. There is no evidence for the overall number density of cluster member X-ray AGN depending on the cluster redshift in a manner different than field AGN, nor there is any evidence that the spatial distribution of cluster AGN (given in units of the cluster overdensity radius r_{500}) strongly depends on the cluster mass or redshift. The $M^{-1.2 \pm 0.7}$ scaling relation we measure is consistent with theoretical predictions of the galaxy merger rate in clusters, which is expected to scale with the cluster velocity dispersion, σ , as $\sim \sigma^{-3}$ or $\sim M^{-1}$. This consistency suggests that AGN in clusters may be predominantly triggered by galaxy mergers, a result that is further corroborated by visual inspection of *Hubble* images for 23 spectroscopically confirmed cluster member AGN in our sample. A merger-driven scenario for the triggering of X-ray AGN is not strongly favored by studies of field galaxies, however, suggesting that different mechanisms may be primarily responsible for the triggering of cluster and field X-ray AGN.

1 INTRODUCTION

Modern studies of galaxy evolution have demonstrated the essential role central supermassive black holes can play in establishing the observed properties of galaxies on both small (~ 1 pc) and large (~ 1 kpc) scales (e.g. Silk & Rees 1998; Ferrarese & Merritt 2000). The powerful outbursts of Active Galactic Nuclei (AGN) appear to be an especially important component of modern galaxy formation models, but many aspects of the connection between galaxies and their AGN remain largely uncertain.

Luminous AGN emit across the entire electromagnetic spectrum, but point-like X-ray emission is one of the cleanest signatures of AGN (Brandt & Hasinger 2005) making X-ray observations particularly well suited for AGN population studies. Deep field surveys of X-ray AGN have already made great progress in understanding the typical host galaxies and environments of AGN. X-ray selected AGN are predominantly hosted in the most massive galaxies, with stellar masses (M_*) of $M_* \gtrsim 10^{10} M_\odot$ (Xue et al. 2010). Compar-

ing the host galaxies of X-ray AGN on the color-magnitude diagram shows that they occupy the same locus of this phase space as normal galaxies with similar stellar masses, suggesting that the host galaxy mass plays the key role in determining the likelihood of it hosting an AGN. This is further supported by investigations into the clustering of X-ray AGN in the field (see Cappelluti et al. 2012, for a review), which indicate that the majority of X-ray AGN are hosted in dark matter halos with masses of $M \sim 10^{13} M_\odot h^{-1}$, a value that is consistently measured out to redshifts of $z \sim 2$.

Although it is clear from these studies that the typical host galaxy environment for an AGN is reasonably well constrained to be self-similar out to redshifts of $z \sim 2$, the triggering mechanism or mechanisms that cause these luminous AGN outbursts remain largely uncertain. Deep field, multiwavelength surveys of X-ray AGN suggest that different mechanisms may dominate for galaxies at different redshifts (see Cappelluti et al. 2012, for a review). Major galaxy mergers are likely the most important mechanisms for fueling quasars at the highest luminosities and redshifts

($L \gtrsim 10^{44}$ erg s $^{-1}$, e.g. Hopkins & Beacom 2006; Hopkins et al. 2008; Hasinger 2008). At lower redshifts ($z \lesssim 1$), bar instabilities and less extreme galaxy-galaxy interactions are inferred to be more efficient at producing AGN (e.g. Georgakakis et al. 2009). Investigations into the properties of the galaxies hosting AGN indicate that their morphologies are similar to comparable galaxies that do not host AGN (e.g. Reichard et al. 2009; Tal et al. 2009).

One useful way to explore these triggering mechanisms is to observe the AGN populations in massive galaxy clusters. Galaxy clusters are not only sites of large numbers of galaxies in close proximity to one another but also host a hot, diffuse, X-ray bright intracluster medium (ICM) (e.g. Sarazin 1988). Both factors are expected to play a role in transforming galaxies in clusters, through tidal encounters, mergers between neighboring galaxies (Mamon 1992; Moore et al. 1998), or by galaxy-ICM interactions such as ram pressure stripping (e.g. Gunn & Gott 1972). Studying how the AGN population in clusters is related to the host cluster properties allows us to understand more completely how the variations in the merger frequency or density of the ICM may influence a galaxy's ability to host an AGN outburst.

Previous studies have established that galaxies in local clusters have lower average star formation rates than the field (e.g. Dressler 1980). Previous studies of the X-ray AGN population in galaxy clusters, however, have typically suffered from limited source statistics. Because the fraction of galaxies hosting X-ray AGN is typically of order $\sim 0.1 - 1\%$ (e.g. Haggard et al. 2010), large samples of galaxy clusters are required to measure the cluster-specific AGN population with high precision. Understanding how the AGN population varies with cluster mass and redshift additionally requires detailed spectroscopy and mass proxy information that is only just becoming available (Mantz et al. 2010a,b; von der Linden et al. 2014; Kelly et al. 2014; Applegate et al. 2014). Finally, any attempt to measure the cluster-specific influences on their constituent AGN population must also account for the cosmic evolution of X-ray AGN in the field (also known as the X-ray Luminosity Function or XLF) which has already been measured to have a strong redshift dependence (e.g. Ueda et al. 2003; Hasinger et al. 2005; Ueda et al. 2014).

In this paper, we expand the analysis of (Ehlert et al. 2013, 2014, hereafter Paper I and Paper II, respectively) to a larger sample of galaxy clusters to test for the presence of a cluster mass and/or redshift dependent signal beyond those expected from field evolution. With more than 11,000 X-ray AGN cataloged here we are able to, for the first time, quantify the extent to which the X-ray AGN population in galaxy clusters may depend on the host cluster mass and redshift. The presence or absence of these signals offers important new evidence as to the key astrophysical processes that drive the evolution of AGN in clusters. When calculating distances, we assume a Λ CDM cosmological model with $\Omega_m=0.3$, $\Omega_\Lambda=0.7$, and $H_0 = 70$ km s $^{-1}$ Mpc $^{-1}$.

2 THE CLUSTER SAMPLE

The clusters included in our study have been drawn from wide-area cluster surveys derived from the *ROSAT* All Sky Survey (Truemper 1993); the *ROSAT* Brightest Cluster Sample (Ebeling et al. 1998); the *ROSAT*-ESO Flux-Limited X-ray Sample (Böhringer et al. 2004); and the MAssive Cluster Survey (Ebeling et al. 2007, 2010). We also included clusters from the 400-Square Degree *ROSAT* PSPC Galaxy Cluster Survey (Burenin et al. 2007). Each sample covers a distinct volume of the Universe: BCS covers the north-

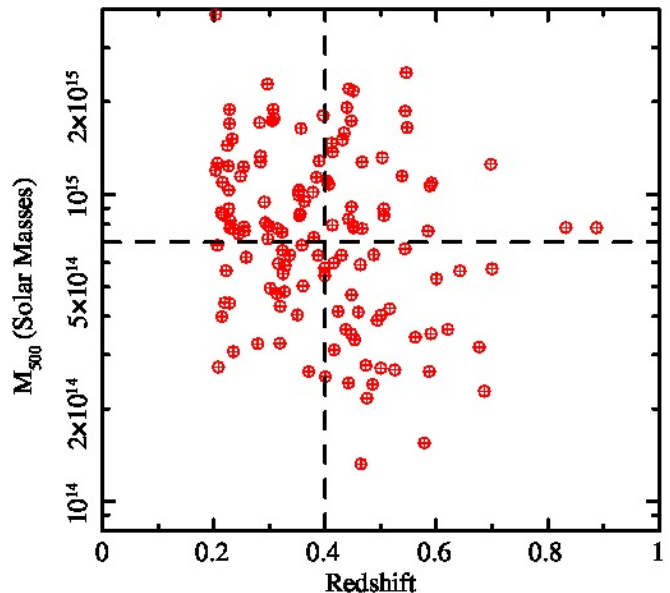


Figure 1. The masses and redshifts of the 135 galaxy clusters in this study. The median cluster redshift of $z = 0.4$ and cluster mass of $M_{500} = 7 \times 10^{14} M_\odot$ are denoted with dashed lines.

ern sky at $z < 0.3$; REFLEX covers the southern sky at $z < 0.3$; and MACS covers higher redshifts, $0.3 < z < 0.9$, at declinations $> -40^\circ$. The 400 deg 2 survey covers high Galactic latitudes at redshifts of $z < 1$. The galaxy clusters included in these samples have been instrumental in recent cosmological studies (Mantz et al. 2008; Vikhlinin et al. 2009; Mantz et al. 2010a,b; Allen et al. 2011). All of the clusters chosen from these samples have *Chandra* exposures of at least 10 ks in public archives as well as robust measurements of their masses and virial radii (Mantz et al. 2010a,b), and are a representative sub-sample of these surveys. In total, 135 unique galaxy clusters are included, with redshifts ranging from $0.2 < z < 0.9$. General information for the clusters and the *Chandra* data sets used may be found in Table 1. We note that these clusters are among the most massive and X-ray luminous clusters in the Universe, and therefore host large numbers of galaxies and substantial masses of hot, X-ray emitting gas (the Intracluster Medium, hereafter ICM). We therefore expect the influences of the local cluster environment to be pronounced in this sample. With measurements of r_{500} available for each cluster, we are able to relate observed trends in the AGN population to the virial radii of the clusters.

Mass measurements and the associated radii, r_{500} , for each cluster are taken from Mantz et al. (2010a,b).¹ The typical uncertainties in measurements of r_{500} are of order 10%. The r_{500} values and X-ray centroids for the clusters are summarized in Table 1, and the distribution of cluster masses and redshifts used for this study are shown in Figure 1.

¹ The scaling radius r_Δ is defined as the radius where the enclosed average mass density is equal to Δ times the critical density of the universe at the cluster's respective redshift, $\rho_c(z)$. The corresponding mass M_Δ is defined as $M_\Delta = 4/3\pi\Delta\rho_c(z)r_\Delta^3$. The mass range extends from $1 \times 10^{14} M_\odot < M_{500} < 5 \times 10^{15} M_\odot$ and the scaling radii range from $0.6 \text{ Mpc} < r_{500} < 2 \text{ Mpc}$.

Table 1. Summary of the cluster sample and *Chandra* observations (either ACIS-I and ACIS-S) listed in order of cluster redshift. A total of 135 clusters of galaxies and 224 independent *Chandra* observations were used. The columns list (1) cluster name; (2) redshift; (3) & (4) right ascension and declination of the cluster X-ray centroid (J2000); (5) the *Chandra* observation number (OBS ID#); (6) observation date; (7) primary detector array used; (8) exposure time in ks, after cleaning; (9) M_{500} for the cluster, in units of $10^{14} M_{\odot}$; (10) r_{500} in Mpc; and (11) the equivalent Galactic hydrogen column density in the direction of the cluster, in units of 10^{20} atoms cm^{-2} . Clusters marked with a † are the clusters included in Paper I.

(1) Cluster Name	(2) z	(3) RA	(4) DEC	(5) OBS ID #	(6) Obs Date	(7) Detector	(8) Exposure (ks)	(9) $M_{500}(10^{14} M_{\odot})$	(10) $r_{500}(\text{Mpc})$	(11) $N_{\text{H}}(10^{20} \text{cm}^{-2})$
Abell 2163	0.203	16 15 45.96	-6 08 53.51	1653	2001-06-16	ACIS-I	71.14	38.5	2.2	15.40
Abell 2163	0.203	16 15 45.96	-6 08 53.51	545	2000-07-29	ACIS-I	9.44	38.5	2.2	15.40
Abell 520	0.203	04 54 9.02	02 55 17.79	4215	2003-12-04	ACIS-I	66.27	11.9	1.5	5.65
Abell 520	0.203	04 54 9.02	02 55 17.79	528	2000-10-10	ACIS-I	9.46	11.9	1.5	5.65
Abell 520	0.203	04 54 9.02	02 55 17.79	7703	2007-01-01	ACIS-I	5.08	11.9	1.5	5.65
Abell 209†	0.206	01 31 53.14	-13 36 48.35	3579	2003-08-03	ACIS-I	9.98	12.6	1.5	1.44
Abell 209†	0.206	01 31 53.14	-13 36 48.35	522	2000-09-09	ACIS-I	9.96	12.6	1.5	1.44
Abell 963†	0.206	10 17 3.56	39 02 51.51	7704	2007-02-18	ACIS-I	5.06	6.8	1.2	1.25
Abell 963†	0.206	10 17 3.56	39 02 51.51	903	2000-10-11	ACIS-S	36.28	6.8	1.2	1.25
RX J0439.0+0520	0.208	04 39 2.18	05 20 42.30	527	2000-08-29	ACIS-I	9.59	2.7	0.9	8.92
RX J0439.0+0520	0.208	04 39 2.18	05 20 42.30	9369	2007-11-12	ACIS-I	19.86	2.7	0.9	8.92
RX J0439.0+0520	0.208	04 39 2.18	05 20 42.30	9761	2007-11-15	ACIS-I	8.65	2.7	0.9	8.92
Abell 1423	0.213	11 57 17.35	33 36 39.75	538	2000-07-07	ACIS-I	9.87	8.7	1.3	1.81
Zwicky 2701	0.214	09 52 49.18	51 53 5.58	3195	2001-11-04	ACIS-S	26.91	4.0	1.0	0.75
RX J1504.1-0248	0.215	15 04 7.58	-2 48 16.30	4935	2004-01-07	ACIS-I	13.29	11.0	1.5	5.97
RX J1504.1-0248	0.215	15 04 7.58	-2 48 16.30	5793	2005-03-20	ACIS-I	39.15	11.0	1.5	5.97
Abell 773	0.217	09 17 52.68	51 43 35.72	3588	2003-01-25	ACIS-I	9.39	8.6	1.3	1.28
Abell 773	0.217	09 17 52.68	51 43 35.72	5006	2004-01-21	ACIS-I	19.81	8.6	1.3	1.28
Abell 773	0.217	09 17 52.68	51 43 35.72	533	2000-09-05	ACIS-I	11.25	8.6	1.3	1.28
RX J0304.1-3656	0.219	03 04 3.26	-36 56 29.54	9413	2008-03-16	ACIS-I	19.86	4.4	1.1	2.30
RX J0237.4-2630	0.222	02 37 27.42	-26 30 27.85	9412	2008-03-03	ACIS-I	18.38	5.6	1.2	1.82
Abell 2261†	0.224	17 22 26.99	32 07 57.89	5007	2004-01-14	ACIS-I	24.31	14.4	1.6	3.19
Abell 2261†	0.224	17 22 26.99	32 07 57.89	550	1999-12-11	ACIS-I	9.06	14.4	1.6	3.19
Abell 1682	0.226	13 06 50.75	46 33 30.25	3244	2002-10-19	ACIS-I	9.77	12.4	1.5	1.04
Abell 2667	0.226	23 51 39.72	-26 04 59.79	2214	2001-06-19	ACIS-S	9.64	9.0	1.4	1.73
RX J0638.7-5358	0.227	06 38 47.29	-53 58 27.67	9420	2008-04-11	ACIS-I	19.89	10.3	1.4	6.06
Abell 1763	0.228	13 35 19.03	40 59 59.40	3591	2003-08-28	ACIS-I	19.59	17.0	1.7	0.82
RX J0220.9-3829	0.228	02 20 56.54	-38 28 51.88	9411	2008-02-29	ACIS-I	19.86	4.4	1.1	1.96
Abell 2219†	0.228	16 40 20.35	46 42 30.00	896	2000-03-31	ACIS-S	42.29	18.9	1.7	1.76
Abell 2111	0.229	15 39 41.13	34 25 7.27	544	2000-03-22	ACIS-I	10.29	7.8	1.3	1.84
Z5247	0.229	12 34 22.11	09 47 4.93	539	2000-03-23	ACIS-I	9.28	8.2	1.3	1.61
Abell 2390†	0.233	21 53 37.08	17 41 45.39	4193	2003-09-11	ACIS-S	95.06	15.2	1.6	6.21
Abell 2390†	0.233	21 53 37.08	17 41 45.39	500	2000-10-08	ACIS-S	9.82	15.2	1.6	6.21
Abell 2390†	0.233	21 53 37.08	17 41 45.39	501	1999-11-05	ACIS-S	9.04	15.2	1.6	6.21
Z2089	0.235	09 00 36.84	20 53 40.36	7897	2006-12-23	ACIS-I	9.04	3.1	0.9	2.86
RX J2129.6+0005†	0.235	21 29 39.73	00 05 18.15	552	2000-10-21	ACIS-I	9.96	7.7	1.3	3.63
RX J2129.6+0005†	0.235	21 29 39.73	00 05 18.15	9370	2009-04-03	ACIS-I	29.64	7.7	1.3	3.63
RX J0439.0+0715	0.244	04 39 0.55	07 16 0.30	1449	1999-10-16	ACIS-I	6.31	7.4	1.3	9.18
RX J0439.0+0715	0.244	04 39 0.55	07 16 0.30	3583	2003-01-04	ACIS-I	19.21	7.4	1.3	9.18
RX J0439.0+0715	0.244	04 39 0.55	07 16 0.30	526	1999-10-16	ACIS-I	1.59	7.4	1.3	9.18
Abell 521†	0.248	04 54 7.42	-10 13 24.29	430	2000-10-13	ACIS-S	39.11	11.4	1.5	4.78
Abell 521†	0.248	04 54 7.42	-10 13 24.29	901	1999-12-23	ACIS-I	38.63	11.4	1.5	4.78
Abell 1835†	0.253	14 01 1.93	02 52 39.89	6880	2006-08-25	ACIS-I	117.91	12.3	1.5	2.04
Abell 1835†	0.253	14 01 1.93	02 52 39.89	6881	2005-12-07	ACIS-I	36.28	12.3	1.5	2.04
Abell 1835†	0.253	14 01 1.93	02 52 39.89	7370	2006-07-24	ACIS-I	39.50	12.3	1.5	2.04
RX J0307.0-2840	0.254	03 07 1.98	-28 39 55.69	9414	2008-03-13	ACIS-I	18.90	7.8	1.3	1.27
Abell 68†	0.255	00 37 5.95	09 09 36.03	3250	2002-09-07	ACIS-I	9.98	7.6	1.3	4.96
MS1455.0+2232	0.258	14 57 15.07	22 20 33.26	4192	2003-09-05	ACIS-I	91.88	6.2	1.2	3.18
MS1455.0+2232	0.258	14 57 15.07	22 20 33.26	543	2000-05-19	ACIS-I	9.85	6.2	1.2	3.18
MS1455.0+2232	0.258	14 57 15.07	22 20 33.26	7709	2007-03-23	ACIS-I	7.06	6.2	1.2	3.18
RX J2011.3-5725	0.279	20 11 27.24	-57 25 10.16	4995	2004-06-08	ACIS-I	23.99	3.3	0.9	4.15
Abell 697†	0.282	08 42 57.62	36 21 57.43	4217	2002-12-15	ACIS-I	19.51	17.1	1.6	2.93
RX J0232.2-4420	0.284	02 32 17.73	-44 20 55.19	4993	2004-06-08	ACIS-I	23.40	12.7	1.5	1.69
RX J0528.9-3927	0.284	05 28 53.25	-39 28 19.12	4994	2004-03-10	ACIS-I	22.45	13.3	1.5	2.10
Zwicky 3146	0.291	10 23 39.64	04 11 12.17	909	2000-05-10	ACIS-I	46.00	9.4	1.3	2.46
Zwicky 3146	0.291	10 23 39.64	04 11 12.17	9371	2008-01-18	ACIS-I	40.16	9.4	1.3	2.46
RX J0043.4-2037	0.292	00 43 24.82	-20 37 24.41	9409	2008-02-02	ACIS-I	19.91	8.1	1.3	1.84
IE0657-56	0.296	06 58 27.55	-55 56 32.44	3184	2002-07-12	ACIS-I	87.47	22.8	1.8	4.89
IE0657-56	0.296	06 58 27.55	-55 56 32.44	4984	2004-08-19	ACIS-I	76.11	22.8	1.8	4.89
IE0657-56	0.296	06 58 27.55	-55 56 32.44	4985	2004-08-23	ACIS-I	27.48	22.8	1.8	4.89
IE0657-56	0.296	06 58 27.55	-55 56 32.44	4986	2004-08-25	ACIS-I	41.48	22.8	1.8	4.89
IE0657-56	0.296	06 58 27.55	-55 56 32.44	5356	2004-08-11	ACIS-I	97.19	22.8	1.8	4.89
IE0657-56	0.296	06 58 27.55	-55 56 32.44	5357	2004-08-14	ACIS-I	79.05	22.8	1.8	4.89
IE0657-56	0.296	06 58 27.55	-55 56 32.44	5358	2004-08-15	ACIS-I	31.95	22.8	1.8	4.89
IE0657-56	0.296	06 58 27.55	-55 56 32.44	5361	2004-08-17	ACIS-I	82.61	22.8	1.8	4.89
IE0657-56	0.296	06 58 27.55	-55 56 32.44	554	2000-10-16	ACIS-I	25.79	22.8	1.8	4.89
Abell 2537†	0.297	23 08 22.00	-2 11 29.75	4962	2004-09-09	ACIS-S	36.19	7.2	1.2	4.62
Abell 2537†	0.297	23 08 22.00	-2 11 29.75	9372	2008-08-11	ACIS-I	38.50	7.2	1.2	4.62
Abell 781	0.298	09 20 25.34	30 30 10.91	534	2000-10-03	ACIS-I	9.94	7.9	1.3	1.65
MACS J2245.0+2637	0.301	22 45 4.56	26 38 4.47	3287	2002-11-24	ACIS-I	16.86	4.9	1.1	5.04

3 *Chandra* DATA REDUCTION AND CATALOG PRODUCTION

All of the galaxy cluster fields were observed with the Advanced CCD Imaging Spectrometer (ACIS) aboard *Chandra*. The data were analyzed using the same analysis procedure discussed in Paper I. This includes the initial processing of each event list, image creation, candidate source detection, and refinement of the source

catalogs using the α point-source analysis package² (Broos et al. 2010). Our α analysis pipeline has three main stages and follows the study of the 4-Ms *CDFS* (Xue et al. 2011), modified to accommodate the higher background rates and shorter exposure times of our cluster observations. Tests discussed in Paper I have shown that our analysis efficiently rejects spurious detections while preserving high completeness. We perform a similar analysis in each

² The *ACIS Extract* software package and User's Guide are available at http://www.astro.psu.edu/xray/acis/acis_analysis.html.

Table 1. Continued

(1)	(2)	(3)	(4)	(5)	(6)	(7)	(8)	(9)	(10)	(11)
Cluster Name	z	RA	DEC	OBS ID #	Obs Date	Detector	Exposure (ks)	$M_{500}(10^{14}M_{\odot})$	r'_{500} (Mpc)	N_{H} (10^{20} cm^{-2})
MACS J2311.5+0338	0.305	23 11 33.17	03 38 7.05	3288	2002-09-07	ACIS-I	13.59	17.4	1.6	4.60
MACS J1131.8-1955	0.306	11 31 55.61	-19 55 45.39	3276	2002-06-14	ACIS-I	13.90	17.6	1.7	4.02
Abell 2744	0.308	00 14 18.75	-30 23 18.04	2212	2001-09-03	ACIS-S	24.81	17.6	1.6	1.39
Abell 2744	0.308	00 14 18.75	-30 23 18.04	7915	2006-11-08	ACIS-I	18.61	17.6	1.6	1.39
Abell 2744	0.308	00 14 18.75	-30 23 18.04	8477	2007-06-10	ACIS-I	45.90	17.6	1.6	1.39
Abell 2744	0.308	00 14 18.75	-30 23 18.04	8557	2007-06-14	ACIS-I	27.81	17.6	1.6	1.39
MS2137.3-2353 [†]	0.313	21 40 15.17	-23 39 39.77	4974	2003-11-13	ACIS-S	57.38	4.7	1.1	3.76
MS2137.3-2353 [†]	0.313	21 40 15.17	-23 39 39.77	5250	2003-11-18	ACIS-S	40.54	4.7	1.1	3.76
MS2137.3-2353 [†]	0.313	21 40 15.17	-23 39 39.77	928	1999-11-18	ACIS-S	43.60	4.7	1.1	3.76
MACS J0242.5-2132	0.314	02 42 35.88	-21 32 26.09	3266	2002-02-07	ACIS-I	11.85	7.7	1.2	2.72
Abell 1995	0.316	14 52 57.96	58 02 56.33	7021	2006-08-30	ACIS-I	48.53	5.9	1.1	1.19
Abell 1995	0.316	14 52 57.96	58 02 56.33	906	2000-05-08	ACIS-S	45.56	5.9	1.1	1.19
MACS J1427.6-2521	0.318	14 27 39.50	-25 21 3.05	3279	2002-06-29	ACIS-I	16.92	3.3	0.9	5.88
MACS J1427.6-2521	0.318	14 27 39.50	-25 21 3.05	9373	2008-06-11	ACIS-I	28.38	3.3	0.9	5.88
MACS J0547.0-3904	0.319	05 47 1.46	-39 04 26.05	3273	2002-10-20	ACIS-I	21.74	4.3	1.0	3.70
MACS J0257.6-2209	0.322	02 57 41.28	-22 09 13.42	3267	2001-11-12	ACIS-I	20.46	7.5	1.2	2.07
MACS J2049.9-3217	0.323	20 49 55.34	-32 16 49.39	3283	2002-12-08	ACIS-I	23.79	6.6	1.2	5.59
MACS J2229.7-2755	0.324	22 29 45.22	-27 55 35.98	3286	2002-11-13	ACIS-I	16.42	5.5	1.1	1.35
MACS J2229.7-2755	0.324	22 29 45.22	-27 55 35.98	9374	2007-12-09	ACIS-I	14.82	5.5	1.1	1.35
MACS J1319.9+7003	0.327	13 20 7.53	70 04 37.21	3278	2002-09-15	ACIS-I	21.62	4.8	1.1	1.24
Zwicky J1358+6245	0.328	13 59 50.90	62 31 2.89	516	2000-09-03	ACIS-S	54.06	5.9	1.1	1.78
MACS J0520.7-1328	0.336	05 20 42.17	-13 28 46.78	3272	2002-02-10	ACIS-I	19.23	6.3	1.2	7.29
CL J0302-0423	0.350	03 02 21.06	-4 23 23.51	5782	2005-12-07	ACIS-I	10.04	4.0	1.0	6.03
MACS J1931.8-2634 [†]	0.352	19 31 49.61	-26 34 33.60	3282	2002-10-20	ACIS-I	13.59	9.9	1.3	8.31
MACS J1931.8-2634 [†]	0.352	19 31 49.61	-26 34 33.60	9382	2008-08-21	ACIS-I	98.92	9.9	1.3	8.31
MACS J0035.4-2015	0.352	00 35 26.22	-20 15 46.12	3262	2003-01-22	ACIS-I	21.35	10.2	1.4	1.64
CL J1212+2733	0.353	12 12 18.40	27 33 1.57	5767	2005-03-17	ACIS-I	14.58	10.3	1.4	1.72
RBS797	0.354	09 47 13.03	76 23 13.93	2202	2000-10-20	ACIS-I	11.74	8.5	1.3	2.28
MACS J1115.8+0129 [†]	0.355	11 15 51.88	01 29 54.98	3275	2003-01-23	ACIS-I	15.90	8.6	1.3	4.34
MACS J1115.8+0129 [†]	0.355	11 15 51.88	01 29 54.98	9375	2008-02-03	ACIS-I	39.62	8.6	1.3	4.34
MACS J0308.9+2645	0.356	03 08 56.03	26 45 34.85	3268	2002-03-10	ACIS-I	24.44	16.4	1.6	9.43
MACS J0404.6+1109	0.358	04 04 32.73	11 08 10.68	3269	2002-02-20	ACIS-I	21.81	6.8	1.2	12.30
RX J0027.6+2616	0.360	00 27 45.55	26 16 21.75	3249	2002-06-26	ACIS-I	9.97	5.0	1.1	3.58
RX J1532.9+3021 [†]	0.363	15 32 53.83	30 20 59.38	1649	2001-08-26	ACIS-S	9.36	9.5	1.3	2.30
RX J1532.9+3021 [†]	0.363	15 32 53.83	30 20 59.38	1665	2001-09-06	ACIS-I	9.97	9.5	1.3	2.30
CL J0318-0302	0.370	03 18 33.27	-3 02 58.36	5775	2005-03-15	ACIS-I	14.57	2.6	0.8	5.30
Zwicky J1953 [†]	0.378	08 50 6.98	36 04 20.45	1659	2000-10-22	ACIS-I	24.86	10.2	1.3	2.96
Zwicky J1953 [†]	0.378	08 50 6.98	36 04 20.45	7716	2006-12-20	ACIS-I	6.98	10.2	1.3	2.96
MACS J0011.7-1523	0.379	00 11 42.83	-15 23 21.69	3261	2002-11-20	ACIS-I	21.60	7.2	1.2	1.85
MACS J0011.7-1523	0.379	00 11 42.83	-15 23 21.69	6105	2005-06-28	ACIS-I	37.27	7.2	1.2	1.85
MACS J0949.8+1708 [†]	0.384	09 49 51.79	17 07 8.31	3274	2002-11-06	ACIS-I	14.31	11.3	1.4	3.08
MACS J1720.2+3536 [†]	0.387	17 20 16.67	35 36 23.35	3280	2002-11-03	ACIS-I	20.84	6.3	1.1	3.46
MACS J1720.2+3536 [†]	0.387	17 20 16.67	35 36 23.35	6107	2005-11-22	ACIS-I	33.88	6.3	1.1	3.46
MACS J1731.6+2252 [†]	0.389	17 31 39.19	22 51 49.96	3281	2002-11-03	ACIS-I	20.50	12.8	1.4	4.99
MACS J2211.7-0349 [†]	0.396	22 11 45.91	-3 49 41.94	3284	2002-10-08	ACIS-I	17.73	18.1	1.6	5.53
MACS J0429.6-0253 [†]	0.399	04 29 36.00	-2 53 5.63	3271	2002-02-07	ACIS-I	23.16	5.8	1.1	4.34
CL J0809+2811	0.399	08 09 41.04	28 12 1.16	5774	2004-11-30	ACIS-I	19.68	5.4	1.1	2.98
V1416-4446	0.400	14 16 28.06	44 46 42.96	541	1999-12-02	ACIS-I	31.15	2.5	0.8	0.76
MACS J1006.9+3200	0.403	10 06 54.69	32 01 30.58	5819	2005-01-24	ACIS-I	10.88	11.1	1.4	1.52
MACS J0159.8-0849	0.406	01 59 49.37	-8 49 59.79	3265	2002-10-02	ACIS-I	17.90	10.8	1.3	2.06
MACS J0159.8-0849	0.406	01 59 49.37	-8 49 59.79	6106	2004-12-04	ACIS-I	35.30	10.8	1.3	2.06
MACS J2228.5+2036 [†]	0.411	22 28 32.78	20 37 14.58	3285	2003-01-22	ACIS-I	19.85	14.7	1.5	4.26
MACS J0152.5-2852	0.413	01 52 33.91	-28 53 33.40	3264	2002-09-17	ACIS-I	17.54	7.9	1.2	1.51
MACS J0159.0-3412	0.413	01 59 20.06	-34 13 6.70	5818	2006-02-19	ACIS-I	9.42	13.7	1.5	1.51
MACS J1105.7-1014	0.415	11 05 45.87	-10 14 35.15	5817	2005-01-03	ACIS-I	10.32	6.0	1.1	4.10
CL J1003+3253	0.416	10 03 4.51	32 53 37.75	5776	2005-03-11	ACIS-I	19.85	3.1	0.9	1.68
MACS J2046.0-3430	0.423	20 46 0.58	-34 30 17.20	5816	2005-06-28	ACIS-I	10.03	4.2	1.0	4.59
MACS J2046.0-3430	0.423	20 46 0.58	-34 30 17.20	9377	2008-06-27	ACIS-I	39.23	4.2	1.0	4.59
MACS J0451.9+0006 [†]	0.429	04 51 54.67	00 06 18.52	5815	2005-01-08	ACIS-I	10.21	6.3	1.1	6.85
MACS J0553.4-3342	0.431	05 53 25.56	-33 42 36.14	5813	2005-01-08	ACIS-I	9.94	15.1	1.5	3.32
MACS J0358.8-2955	0.434	03 58 53.38	-29 55 44.00	11719	2009-10-18	ACIS-I	9.64	15.8	1.5	0.98
MACS J1226.8+2153	0.437	12 26 51.04	21 49 54.98	12878	2011-04-11	ACIS-I	129.97	0.0	0.9	1.66
MACS J1226.8+2153	0.437	12 26 51.04	21 49 54.98	3590	2003-12-13	ACIS-I	19.00	3.6	0.9	1.66

of three energy bands: a soft band (0.5 – 2.0 keV), a hard band (2.0 – 8.0 keV), and the full band (0.5 – 8.0 keV).

Every cluster field was subsequently inspected visually to ensure that candidate sources associated with cluster substructure were removed from the analysis. Since cold fronts, cool cores, and cavities associated with mechanical feedback from AGN are all sources of potential surface brightness fluctuations on spatial scales comparable to *Chandra* PSF, these regions can only be rejected reliably by such visual inspection. We adopt the same criterion for inclusion in the final catalog as in Paper I, including all sources that satisfy a no-source binomial probability threshold of $P_b < 10^{-3}$ in any of the three energy bands. A total of 11671 sources satisfy this threshold.

11328, 9244, and 7128 sources satisfy $P_b < 10^{-3}$ in the full band, soft band, and hard band, respectively, and 5448 sources satisfy this same threshold in all three bands. The majority of these sources are detected in more than one energy band. Only 747, 247,

and 96 sources are detected exclusively in the full band, soft band, and hard band respectively.

3.1 Sensitivity Maps

Determinations of the local flux limit to which we can robustly identify a point source, commonly known as the sensitivity map, were performed in an identical manner to that discussed in Paper I. In short, our procedure solves for the number of counts required to satisfy our no-source binomial probability threshold, $P_b < 10^{-3}$, for each position in the field of view. Our procedure takes into account PSF broadening with off-axis angle, variations in the effective exposure time (due to vignetting and CCD chip gaps, for example), and variations in the background across the field of view, including the diffuse galaxy cluster emission.

Only a small number of sources in the final catalog have measured full-band fluxes below the flux limit at their respective positions (371/10246 ~ 3.6%). In the majority of these cases, the flux

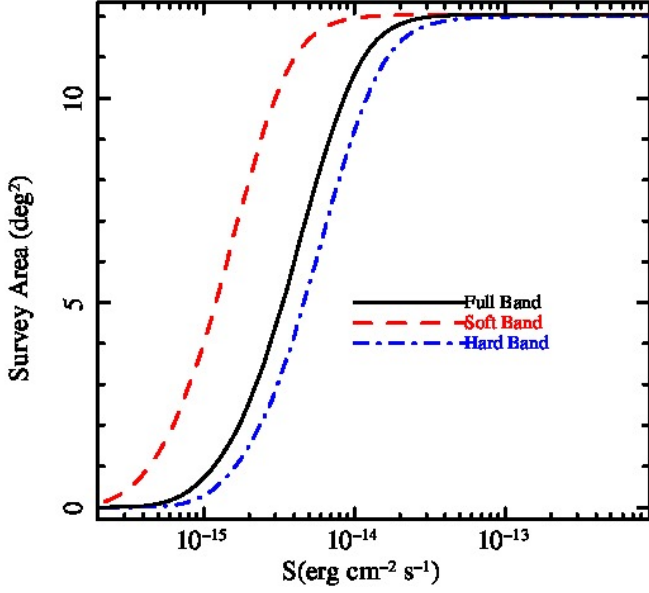


Figure 2. Survey solid angle as a function of flux limit in the soft, hard, and full bands for all cluster observations. We only include the central 12 arcminutes of each pointing in calculating the $\log N - \log S$ and radial profiles, in order to ensure sample completeness. The total survey area over these 135 clusters is 12.0 deg².

measurements are consistent with the flux limits within statistical uncertainties. Only 128 (1.2%) of the point sources in the final catalog have a measured flux inconsistent with the local flux limit at their respective positions at a level greater than 68% confidence.³ It can be expected that some sources will have such characteristics, given differences in the spectra of the point sources relative to the assumed AGN spectrum (a power-law with photon index of $\Gamma = 1.4$). Indeed, those sources that are fainter than their local flux limits for which successful spectral fits were obtained are measured to be significantly softer than our canonical AGN source. General information about the point source catalogs and sensitivity maps for each cluster can be found in Table 1. The total survey area sensitive to different flux levels is shown in Figure 2. In order to ensure that our sample is reliably complete, we restrict ourselves to the central 12 arcminutes of each field of view.

4 RESULTS ON CLUSTER AGN COUNTS AND SPATIAL DISTRIBUTION

Our final point source catalogs and sensitivity maps determine the distribution of X-ray bright AGN across the cluster fields. In all cases, the dominant uncertainty in our measurements is the Poisson uncertainty in the measured number of sources. The expected Poisson fluctuations for samples of size n are estimated using the $1-\sigma$ asymmetric confidence limits of (Gehrels 1986). The $1-\sigma$ upper confidence limit λ_U and $1-\sigma$ lower confidence limit λ_L for a sample of n sources are approximated as

$$\lambda_U(n) = n + 1 + \sqrt{0.75 + n}$$

³ Uncertainties on the source fluxes are estimated at the $\sim 30\%$ level. This is the typical uncertainty in the flux measured from spectral fits to these sources using XSPEC.

Table 1. Summary of X-ray point source numbers and flux limits for each cluster field. The columns list (1) cluster name; (2) the number of AGN satisfying $P_b < 10^{-3}$ in the soft band, the hard band, the full band, and in any band, respectively; (3) the flux limit for each cluster observation in the soft, hard, and full bands, defined as the minimum flux to which 50% of the survey area is sensitive, in units of $\times 10^{-15}$ erg cm⁻² s⁻¹. Observations denoted with an ^a utilize a mix of ACIS-S and ACIS-I observations.

Cluster Name	$N_{\text{soft}}/N_{\text{hard}}/N_{\text{full}}/N_{\text{any}}$	Flux Limit
Abell 2163	68/57/83/90	1.12/3.55/2.82
Abell 520	95/78/121/133	1.26/5.62/3.98
Abell 209	36/33/50/56	2.00/6.31/5.01
Abell 963 ^a	61/45/75/79	2.51/14.13/8.91
RX J0439.0+0520	76/72/103/107	1.26/5.01/3.98
Abell 1423	27/18/33/39	2.82/10.00/7.08
Zwicky 2701	49/29/58/62	1.26/5.01/3.55
RX J1504.1-0248	73/54/88/93	1.12/4.47/3.16
Abell 773	72/72/96/103	1.78/7.08/5.01
RX J0304.1-3656	40/30/55/59	1.78/7.08/5.01
RX J0237.4-2630	43/31/53/54	2.00/7.94/5.62
Abell 2261	59/48/68/75	1.58/5.62/3.98
Abell 1682	33/24/40/51	3.55/12.59/10.00
Abell 2667	23/19/29/34	3.16/11.22/7.94
RX J0638.7-5358	44/36/54/60	2.00/7.08/5.01
Abell 1763	47/38/59/64	2.00/6.31/5.01
RX J0220.9-3829	52/41/63/65	1.78/7.08/5.01
Abell 2219	31/18/34/40	1.26/4.47/3.16
Abell 2111	38/19/46/50	3.16/10.00/7.94
Z5247	30/21/36/36	3.55/11.22/7.94
Abell 2390	69/54/88/93	1.58/10.00/5.62
Z2089	29/19/37/37	2.82/11.22/7.94
RX J2129.6+0005	81/54/99/109	1.78/7.08/5.01
RX J0439.0+0715	59/42/69/86	2.51/10.00/7.08
Abell 521 ^a	110/81/133/141	1.00/4.47/3.16
Abell 1835	137/115/171/177	0.79/3.16/2.51
RX J0307.0-2840	55/29/61/65	2.00/7.08/5.01
Abell 68	36/30/47/50	2.82/10.00/7.08
MS1455.0+2232	130/96/142/158	0.89/3.55/2.51
RX J2011.3-5725	65/57/79/82	1.41/5.62/3.98
Abell 697	51/42/66/69	1.78/6.31/5.01
RX J0232.2-4420	42/35/55/58	1.78/7.08/5.01
RX J0528.9-3927	64/37/67/72	1.78/7.08/5.01
Zwicky 3146	111/78/128/140	1.12/4.47/3.16
RX J0043.4-2037	46/29/54/58	1.78/7.08/5.01
1E0657-56	267/196/309/340	0.50/2.24/1.41
Abell 2537 ^a	80/63/100/104	1.12/5.01/3.55
Abell 781	34/21/37/41	3.16/8.91/7.08
MACS J2245.0+2637	44/39/59/62	1.78/7.08/5.01
MACS J2311.5+0338	37/21/46/50	2.51/10.00/7.08
MACS J1131.8-1955	46/28/58/59	2.24/7.94/6.31
Abell 2744 ^a	120/98/150/159	1.26/5.01/3.55
MS2137.3-2353	54/44/66/68	0.56/2.82/1.78
MACS J0242.5-2132	28/20/36/37	2.51/8.91/6.31
Abell 1995	118/83/138/148	0.89/3.55/2.51
MACS J1427.6-2521	75/65/91/93	1.00/10.00/7.08
MACS J0547.0-3904	61/44/73/77	1.41/5.62/3.98
MACS J0257.6-2209	55/41/70/72	1.58/5.62/3.98

$$\lambda_L(n) = n \left(1 - \frac{1}{9n} - \frac{1}{3\sqrt{n}} \right)^3$$

These estimates are accurate to within a few percent for all values of n . Monte Carlo simulations estimating the impact of uncertainties in the source flux measurements and systematic uncertainties

Table 1. Continued

Cluster Name	$N_{\text{soft}}/N_{\text{hard}}/N_{\text{full}}/N_{\text{any}}$	Flux Limit
MACS J2049.9-3217	49/43/67/73	1.41/5.01/3.98
MACS J2229.7-2755	55/37/62/66	1.26/5.01/3.55
MACS J1319.9+7003	58/46/74/78	1.78/7.08/4.47
Zwicky J1358+6245	67/40/73/84	0.79/3.55/2.24
MACS J0520.7-1328	49/32/60/65	1.58/6.31/4.47
CL J0302-0423	28/25/38/42	2.51/11.22/7.08
MACS J1931.8-2634	104/92/133/137	0.63/2.51/1.78
MACS J0035.4-2015	46/40/59/61	1.58/5.62/3.98
CL J1212+2733	40/34/54/56	2.24/7.94/5.62
RBS 797	46/26/52/54	2.24/7.94/5.62
MACS J1115.8+0129	76/63/92/94	0.89/3.55/2.51
MACS J0308.9+2645	38/30/46/52	1.58/5.62/3.98
MACS J0404.6+1109	44/36/56/57	1.41/5.62/3.98
RX J0027.6+2616	23/19/32/36	2.51/10.00/7.08
RX J1532.9+3021 ^a	37/24/41/46	2.00/7.08/6.31
CL J0318-0302	43/31/51/54	2.00/7.94/5.62
Zwicky 1953	83/51/101/106	1.41/5.62/3.98
MACS J0011.7-1523	106/93/135/144	1.41/5.62/3.98
MACS J0949.8+1708	39/34/48/49	2.24/7.08/5.62
MACS J1720.2+3536	100/81/119/125	0.89/3.55/2.82
MACS J1731.6+2252	64/48/79/83	1.58/5.62/4.47
MACS J2211.7-0349	53/43/73/80	1.78/7.08/5.01
MACS J0429.6-0253	68/58/87/91	1.41/5.62/3.98
CL J0809+2811	36/26/47/52	1.78/7.08/5.01
V1416+4446	68/48/83/94	1.12/4.47/3.16
MACS J1006.9+3200	45/31/54/55	2.51/10.00/6.31
MACS J0159.8-0849	64/50/81/88	1.12/5.62/3.16
MACS J2228.5+2036	60/51/75/78	1.58/6.31/4.47
MACS J0152.5-2852	37/32/47/48	1.78/6.31/4.47
MACS J0159.0-3412	39/32/45/47	2.82/11.22/7.94
MACS J1105.7-1014	35/25/42/44	2.51/10.00/7.08
CL J1003+3253	56/39/66/69	1.78/6.31/4.47
MACS J2046.0-3430	72/64/89/91	0.89/3.55/2.51
MACS J0451.9+0006	39/31/50/52	2.82/10.00/7.08
MACS J0553.4-3342	23/18/35/37	2.82/10.00/7.08
MACS J0358.8-2955	24/23/36/37	3.16/11.22/7.94
MACS J1226.8+2153	119/111/154/76	1.78/6.31/4.47
MACS J1206.2-0847	59/53/84/86	1.41/5.01/3.98
CL J0141-3034	55/44/70/74	1.26/5.01/3.55
IRAS09104	22/18/29/32	2.51/11.22/7.08
MACS J0417.5-1154	100/87/125/131	1.00/4.47/4.47
MACS J2243.3-0935	48/38/58/62	1.78/5.62/4.47
MACS J0455.2+0657	41/23/48/49	2.51/10.00/7.08
MACS J1359.1-1929	34/23/43/44	2.51/10.00/7.08
MACS J0326.8-0043	25/15/34/36	2.51/10.00/7.08
MACS J0329.6-0211	74/62/94/102	0.89/3.55/2.51
RX J1347.5-1145	57/56/79/86	1.00/5.01/2.82
MACS J0140.0-0555	31/18/36/36	2.51/10.00/7.08
V1701+6414	63/51/80/84	1.00/3.55/2.51
3C295	122/101/145/153	0.56/2.51/1.58
MACS J1621.3+3810	134/112/154/159	0.71/2.82/2.00
CL J1641+4001	83/74/97/100	0.89/3.55/2.51
MACS J1115.2+5320	78/61/96/104	2.00/7.94/5.62
MACS J1108.8+0906	57/46/76/80	1.26/5.01/3.55
CL J0355-3741	42/34/50/56	1.41/5.62/3.55
CL J0333-2456	68/57/89/93	1.00/4.47/3.16
MACS J0111.5+0855	66/52/78/79	1.58/5.62/3.98

Table 1. Continued

Cluster Name	$N_{\text{soft}}/N_{\text{hard}}/N_{\text{full}}/N_{\text{any}}$	Flux Limit
MACS J1427.2+4407	72/61/93/95	1.00/3.98/2.82
MACS J1311.0-0310	135/113/168/177	1.00/3.98/2.82
CL J1002+6858	41/39/57/62	1.58/6.31/4.47
RX J003033.2+261819	47/32/57/60	1.78/7.08/5.01
MACS J2214.9-1359	79/58/99/104	1.12/4.47/3.16
MACS J0911.2+1746	71/49/81/88	1.00/3.98/2.82
MACS J0257.1-2325	78/56/95/106	1.26/5.01/3.55
V1525+0958	71/52/87/94	1.00/3.16/2.51
CL J1357+6232	70/61/93/97	0.89/3.55/2.51
MACS J0454.1-0300 ^a	66/45/75/85	2.24/7.94/6.31
MACS J1423.8+2404 ^a	103/83/121/127	1.41/7.08/4.47
MACS J1149.5+2223	80/65/99/107	2.24/7.94/6.31
MACS J0717.5+3745	127/92/141/156	1.00/3.98/2.82
MS0015.9+1609	90/78/109/116	0.63/2.51/1.78
V1121+2327	108/90/131/135	0.63/2.51/1.78
CL J0216-1747	98/74/114/123	0.89/5.01/3.55
MACS J0025.4-1222	142/111/168/182	0.89/4.47/2.82
CL J0956+4107	90/65/112/118	1.00/3.98/2.82
MACS J2129.4-0741	85/67/101/106	1.12/4.47/3.16
CL0328-2140	71/66/95/100	0.89/3.55/2.51
MACS J0647.7+7015	68/50/89/91	1.12/4.47/3.16
CL J1120+4318	56/38/70/74	1.58/6.31/4.47
CL J1334+5031	49/45/70/70	2.00/7.08/5.01
CL J0542.8-4100	113/72/127/136	0.89/3.16/2.24
CL J1202+5751	77/72/102/108	0.79/3.16/2.24
CL J0405-4100	82/68/101/112	1.26/5.62/3.98
MACS J0744.8+3927	104/95/130/139	0.71/3.16/2.24
V1221+4918	103/95/139/149	0.63/2.51/1.78
CL J0152.7-1357	95/65/116/121	1.12/3.98/2.82
CL J1226.9+3332 ^a	109/84/128/131	1.00/4.47/3.55

in the sensitivity maps show that these uncertainties are negligible compared to the Poisson uncertainties on the source counts.

We have compared our results on the X-ray point source population in the cluster fields to both the *CDFS* and the *Chandra COSMOS* deep field surveys (Elvis et al. 2009; Puccetti et al. 2009). In order to minimize the effects of differences in the analysis pipelines and calibration products used, the *COSMOS* results presented here are the result of a re-analysis of those data using our pipeline and with measurements made in the same energy bands. The analysis of the *CDFS* fields used a pipeline similar to ours, and no re-analysis was required to enable a direct comparison. Unless otherwise noted, all numbers and fluxes listed correspond to the full band catalog, and have been corrected for Galactic absorption.

4.1 Cumulative Number Counts

The cumulative number density of sources above a given flux (S) is calculated as

$$N(> S) = \sum_{S_i > S} \frac{1}{\Omega_i} \quad (1)$$

where Ω_i is the total survey area sensitive to the i^{th} source flux S_i . The $\log N - \log S$ cumulative number counts for sources in the full, soft, and hard energy bands are shown in Figure 3, together with a comparison to the *CDFS* and *COSMOS* results in the same bands (Lehmer et al. 2012). The cumulative number counts for the cluster and field sources show the commonly observed broken power-law shape (Cowie et al. 2002; Moretti et al. 2003; Bauer et al. 2004;

Lehmer et al. 2012). Above fluxes of $\sim 10^{-14}$ erg cm $^{-2}$ s $^{-1}$, the cluster fields exhibit a slight excess in source density compared to field surveys. These results are consistent with and build on those discussed in Paper I, and demonstrate the robustness of this analysis procedure.

4.2 The Radial Distribution of X-ray Sources

The spatial distribution of point sources about the cluster centers has been calculated for all point sources with full-band fluxes above 1×10^{-14} erg cm $^{-2}$ s $^{-1}$. Similar analyses were performed in the soft band and hard bands, with flux limits of 3×10^{-15} erg cm $^{-2}$ s $^{-1}$ and 10^{-14} erg cm $^{-2}$ s $^{-1}$, respectively. The full band flux limit corresponds to a luminosity of $\sim 10^{42}$ erg s $^{-1}$ for the lowest redshift cluster in this sample (Abell 2163) and $\sim 10^{43}$ erg s $^{-1}$ for the highest redshift cluster (CL J1226.9+3332).

The adoption of these flux limits minimizes complications due to residual incompleteness and systematic uncertainties in the sensitivity maps, while maintaining a strong statistical signal. A total of 6443, 3055, and 2933 sources satisfy these criteria in the full, soft, and hard bands, respectively. The projected radial distributions are plotted in Figure 4 as a function of radius in units of r_{500} . The projected radii of sources in each cluster field were calculated assuming that they lie at the cluster redshift. The projected source density profile and its statistical uncertainties in each radial bin are calculated in an identical manner to that used to calculate the cumulative number counts.

In this representation, we find clear evidence for an excess of point sources in the central regions of the clusters. At large radii, the measured source number densities converge to an approximately constant source density. Fitting the number density of full (0.5 – 8.0 keV) band sources between 3-5 r_{500} with a constant model provides an estimated background number density of 311 ± 16 deg $^{-2}$.⁴ The measured value is also in agreement with the expected background source density from the *CDFS* and *COSMOS* studies within statistical uncertainties. Within the projected central virialized cluster region ($\sim 2r_{500}$), the constant background density model provides a poor fit to the point source density, and can be rejected at $> 99.9\%$ confidence. The results of the background fits in all three bands are shown in Table 2. The high statistical precision of our data enable us to measure an excess of approximately 3 sources per cluster field within 2 r_{500} in each energy band. We do not expect any significant contribution to this signal from gravitational lensing given the results of (Refregier & Loeb 1997) and Gilmour et al. (2009). In fact, given the shape of the cumulative number counts ($\log N - \log S$), gravitational lensing is expected to suppress the detection of sources near the centers of clusters (Refregier & Loeb 1997; Gilmour et al. 2009).

We have fitted the observed X-ray point source density profiles in all three bands with a King-law+Constant model:

$$N_X(r) = \frac{N_0}{1 + \left(\frac{r}{r_c}\right)^2} + C_X \quad (2)$$

where r_c is the core radius of the fit. The resulting posterior distributions for the fits in each energy band are nearly identical to one another. In each case, we measure a median core radius of $r_c = 1.2 r_{500}$, with a 68% confidence interval spanning the range of $r_c \in [0.7, 2.1] r_{500}$. Most published studies of the optical galaxy

⁴ The constant model provides a statistically acceptable fit to the data ($\chi^2 = 4.7$ for $\nu = 7$ degrees of freedom).

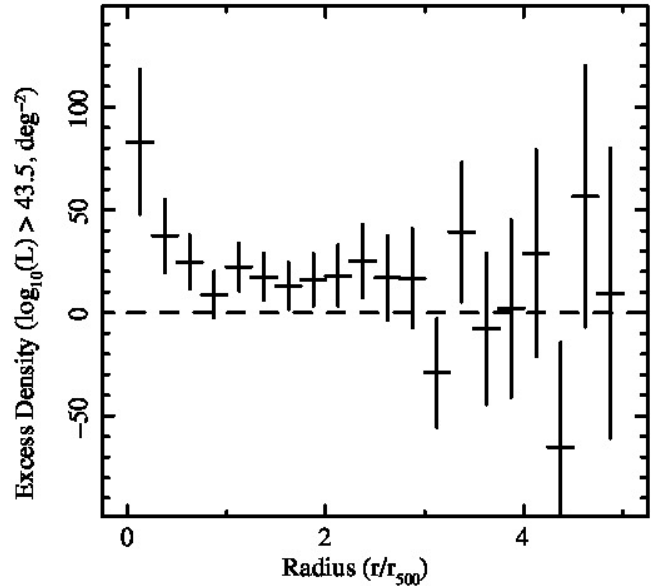


Figure 5. The projected density of X-ray point sources detected above a full band luminosity limit of $L \geq 3 \times 10^{43}$ erg s $^{-1}$, in units of deg $^{-2}$. This projected source density follows the same power-law model as that observed for the flux-limited sample.

population in clusters measure the projected galaxy density profile to follow a King Model or NFW model with a scale radius of $\sim 0.2 - 0.5 r_{500}$ (Popesso et al. 2007; Budzynski et al. 2012). King models with core radii $r_c < 0.5 r_{500}$ can be rejected at $\gtrsim 99\%$ confidence. This indicates that the fraction of cluster member galaxies hosting X-ray AGN rises with radius (see also Paper II). Fitting the observed X-ray point source density profile to a power-law model ($N_X(r) \sim r^\beta$) gives similar results as in Paper I: we measure a median power-law index of $\beta = -0.5 \pm 0.1$ consistently across all three energy bands.

4.2.1 The Distribution of Luminous Cluster Member AGN

We have also determined the radial distribution of X-ray point sources above the field using a full band luminosity limit of $L \geq 3 \times 10^{43}$ erg s $^{-1}$ after a statistical subtraction of the field population. For each cluster we determined the flux limit corresponding to $L = 3 \times 10^{43}$ erg s $^{-1}$ at the cluster redshift, and then calculated for each radial bin the number of sources detected and number of expected field sources⁵ brighter than that flux limit. The projected number density of excess sources above this luminosity limit is given by the difference of these two values in each radial bin, divided by the total survey area. We use Monte Carlo simulations to determine the error bars on each of these measurements.

Our calculations show that these luminous AGN are distributed out to distances of $\sim 2.5r_{500}$, beyond which the excess number density is consistent with zero. Fitting this profile to a power-law model provides a best-fit logarithmic slope of $-0.5 < \beta < -0.6$, which is consistent with the power-law slope measured for the flux limited sample without statistical field subtraction. The measured excess corresponds to a total of ~ 1 excess sources with $L_X \geq 3 \times 10^{43}$ erg s $^{-1}$ per cluster.

⁵ We use our determinations of the *COSMOS* $\log N - \log S$ to determine the number of sources expected from the field in each radial bin.

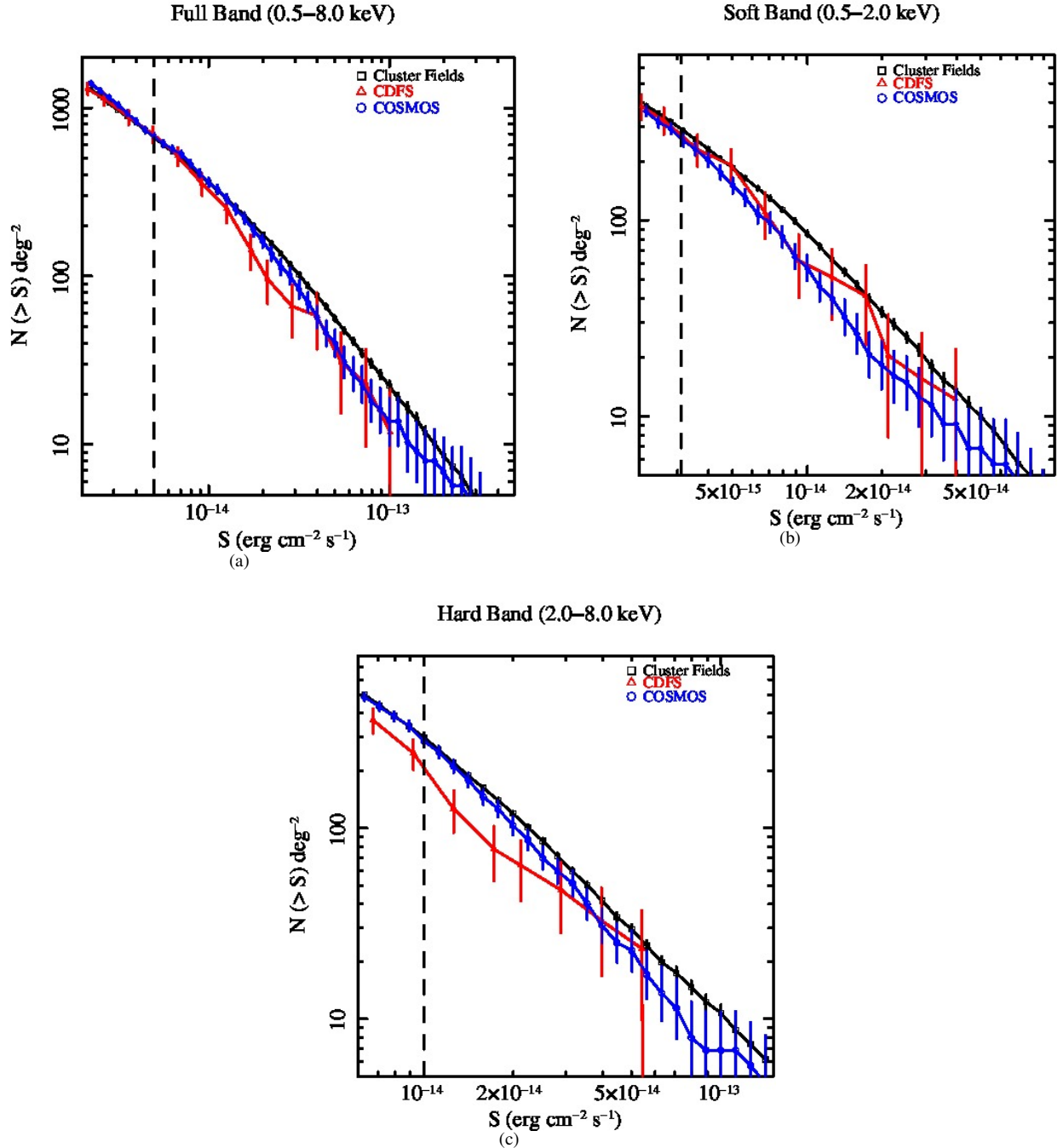


Figure 3. Cumulative number counts ($\log N - \log S$) in the full (0.5 – 8.0 keV, a), soft (0.5 – 2.0 keV, b), and hard (2.0 – 8.0 keV, c) energy bands for the cluster fields (black). The red curves show the cumulative number counts in the same energy bands for the *CDFS*. The blue curves are the results from the *COSMOS* survey. The band-specific flux limits used to determine the radial distribution of X-ray point sources are denoted by the vertical dashed line in each figure. In all three bands an excess of sources at fluxes $\gtrsim 10^{-14} \text{ erg cm}^{-2} \text{ s}^{-1}$ with respect to the control fields is observed.

Using this same luminosity limit, we also determined the co-moving number density of cluster member X-ray AGN within $2r_{500}$ in each of our 135 galaxy clusters in Figure 6 after statistical field subtraction. Although the statistical significance of any individual cluster’s excess AGN density is small, there is nevertheless evidence for lower overall number densities of AGN in more massive clusters.

5 TESTING MASS AND REDSHIFT DEPENDENT MODELS

Such a large and well-characterized sample allows us to measure the specific evolution of cluster AGN versus that in the field. To this end, we utilize a Markov Chain Monte Carlo (MCMC) analysis procedure to determine posterior probability distributions for parameters in a redshift, luminosity, and cluster mass dependent model for the projected point source density profile. We confront

Table 2. Flux limits for the radial profiles and the expectations for the X-ray point source density from *CDFS* and *COSMOS* deep fields in all three energy bands. The columns list: (1) the energy band; (2) the flux limit used in constructing the radial profile fits, in units of $\text{erg cm}^{-2} \text{s}^{-1}$; (3) the measured background density between 3 and 5 r_{500} from the radial profile; (4) the number of sources detected within $2r_{500}$ at that flux limit, across all clusters; (5) the survey area within $2r_{500}$ at that flux limit, in units of deg^{-2} ; (6) the average excess number of sources per cluster above that flux limit within $2r_{500}$, determined by extrapolating measurements of the field density from the best-fit constant model between 3 and 5 r_{500} ; (7) the best-fit power-law index for the projected source density of cluster member AGN; (8) the density of field sources from the *CDFS* at that flux limit; and (9) the density of field sources from *COSMOS* at that flux limit.

(1) Band	(2) Flux Limit	(3) Cluster Fields (deg^{-2})	(4) n_2	(5) Ω_2 (deg^2)	(6) Excess	(7) β	(8) <i>CDFS</i> (deg^{-2})	(9) <i>COSMOS</i> (deg^{-2})
Full	1×10^{-14}	311 ± 16	2474	6.6	3.1 ± 0.5	-0.42 ± 0.12	330 ± 48	356 ± 21
Soft	3×10^{-15}	263 ± 14	2683	8.8	2.8 ± 0.4	-0.53 ± 0.22	250 ± 45	255 ± 18
Hard	1×10^{-14}	244 ± 14	2595	8.5	3.1 ± 0.4	-0.48 ± 0.14	220 ± 45	287 ± 19

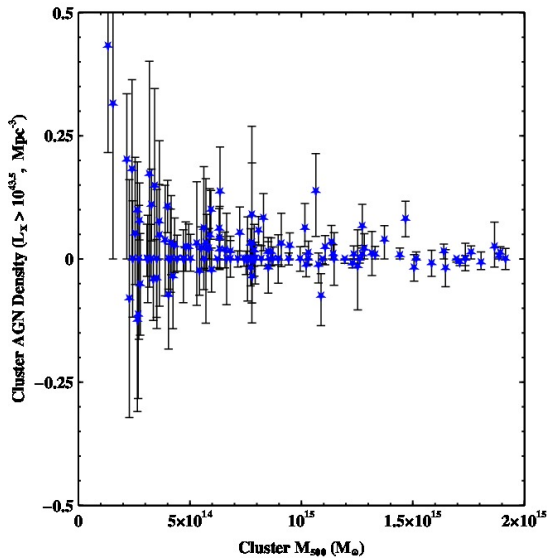


Figure 6. The comoving number density of X-ray AGN more luminous than $3 \times 10^{43} \text{ erg s}^{-1}$ within $2r_{500}$ for our cluster sample, as a function of cluster mass M_{500} . These number densities were determined by statistically subtracting the expected number of field sources in each cluster aperture using the field AGN density as determined by *COSMOS* from the number of sources we detect; hence negative AGN densities are possible. While only a few of the clusters have excesses that are individually larger than zero with high statistical significance, there is nevertheless evidence that lower mass clusters host larger AGN densities within $2r_{500}$ as compared to more massive clusters.

our model with the data from each of the 135 galaxy clusters, marginalizing over uncertainties in the expected evolution of X-ray AGN in the field and the density of background sources expected in our survey.⁶ More specifically, our model assumes that the projected number density of cluster sources (in units of deg^{-2}) above a given flux limit f , at a redshift z and projected distance r from the center of a cluster of mass M_{500} , is proportional to the co-moving number density of X-ray AGN in the field at the cluster redshift

⁶ By background sources, we mean X-ray point sources coincident with the cluster along the line of sight that are not at the cluster redshift. These sources have been shown to have a roughly constant density across survey areas as large as $\sim 1 \text{ deg}^2$ (Xue et al. 2011; Elvis et al. 2009).

(known as the X-ray Luminosity Function or XLF) with a power-law spatial dependence:

$$N_{\text{obs}}(> f, r, z) = N \times D_A(z)^2 \times r_{500} \times \Phi(> L_{\text{cut}}, z) \times \left(\frac{r}{r_{500}}\right)^\beta + C \quad (3)$$

where $\Phi(> L_{\text{cut}}, z)$ is the expected co-moving number density (in units of Mpc^{-3}) of X-ray AGN at that redshift in the luminosity range of $L_{\text{cut}} < L < 10^{46} \text{ erg s}^{-1}$ as determined by the XLF model of Ueda et al. (2014). The lower limit of the luminosity function L_{cut} is the intrinsic luminosity of an AGN at the cluster redshift corresponding to the survey flux cut-off f in the survey of $10^{-14} \text{ erg cm}^{-2} \text{ s}^{-1}$. This flux cut-off corresponds to a luminosity range of $\sim 10^{42-43} \text{ erg s}^{-1}$ for the cluster member AGN. We assume that the cluster AGN contribution arises within a cylinder, centered on the cluster, whose line-of-sight depth scales with r_{500} . $D_A(z)$ is the angular diameter distance specific to each cluster. The parameter N includes the necessary unit conversions and describes the factor by which the number density of AGN in clusters exceeds the field value specified by the XLF (hereafter the scaling factor). C is the (constant) density of field AGN at our flux limit f . We allow the scaling factor to vary as a power law in mass and redshift

$$N \rightarrow N_0(1+z)^\eta \left(\frac{M_{500}}{10^{15} M_\odot}\right)^\xi \quad (4)$$

and also allow the radial distribution to depend linearly on the cluster mass and redshift as

$$\beta \rightarrow \beta_0 + \beta_z(1+z) + \beta_m \left(\frac{M_{500}}{10^{15} M_\odot}\right) \quad (5)$$

Our null hypothesis is that the AGN population in clusters scales with the expected field behavior (i.e. the cluster AGN population evolves in a scaled manner with respect to the field AGN population across all redshifts and for clusters of all masses), which in terms of our model means that all mass and redshift dependent terms (i.e. ζ, η, β_z & β_m) should be statistically consistent with 0.

Our MCMC analysis provides several key advantages over a more traditional statistical analysis, in particular: 1) It uses the full information of cluster redshifts and masses without the need to resort to binning; 2) we are able to interpret the results within the context of our complex selection function, which varies the overall luminosity limit from cluster to cluster as well the area in each radial bin sensitive to sources of a given flux; and 3) we are able to determine robustly the covariances between the different model parameters, which are difficult to anticipate *a priori*.

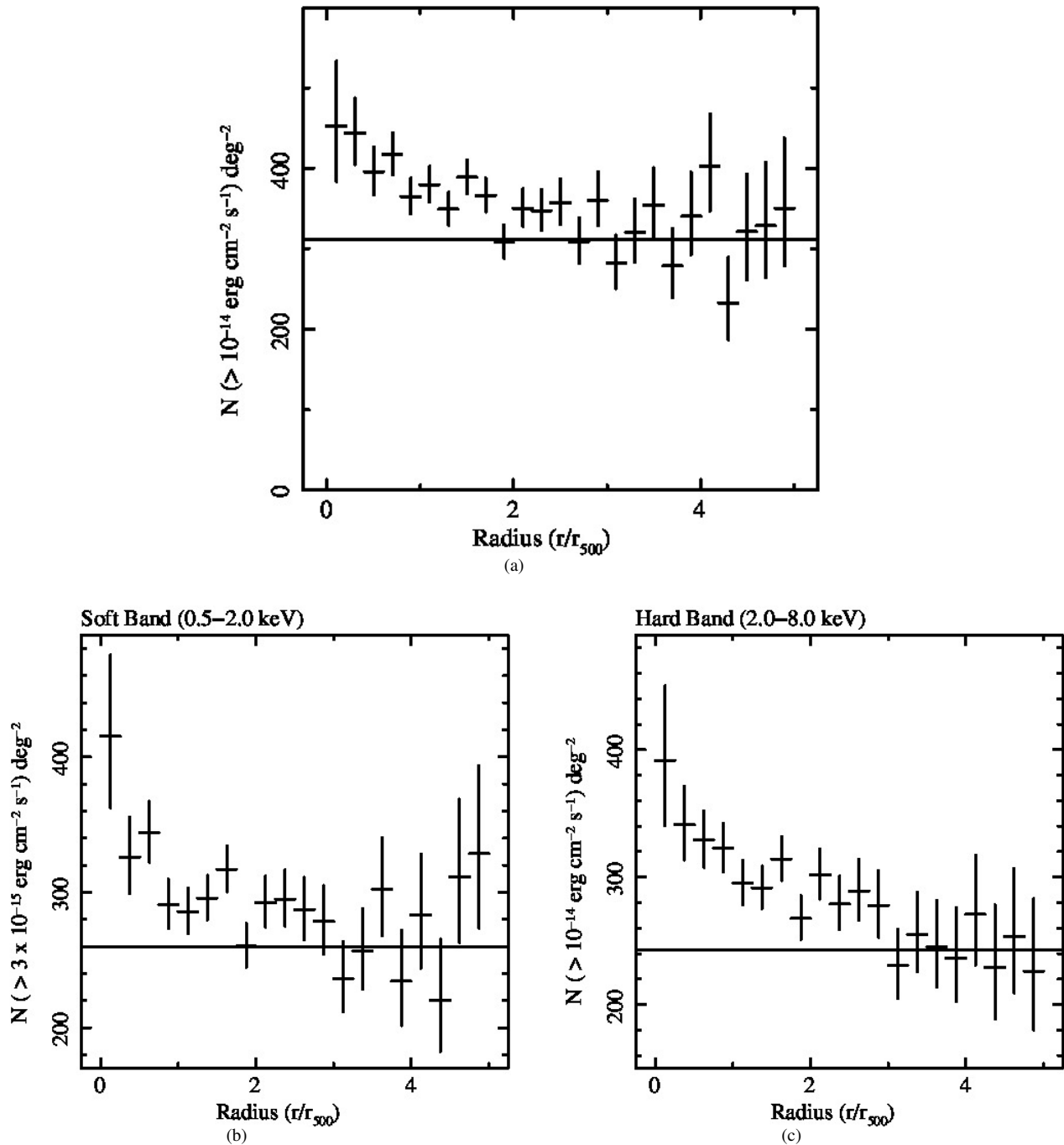


Figure 4. The projected density of X-ray bright point sources in all three bands, in units of deg^{-2} . In all three lines, the solid black line corresponds to the best-fit constant background density in the range 3–5 r_{500} , and in all three cases this background density is consistent with the expected field source density derived from *CDFS* and *COSMOS*. In all three energy bands, this constant background field density is consistent with the expected field density determined from the *CDFS* and *COSMOS* data. (a): The surface density of X-ray bright full band sources ($F_X(0.5 - 8.0 \text{ keV}) > 1 \times 10^{-14} \text{ erg cm}^{-2} \text{ s}^{-1}$) as a function of radius, in units of r_{500} . A total of 2675 sources were included in the calculation of this profile. (b): The surface density of X-ray bright soft band sources ($F_X(0.5 - 2.0 \text{ keV}) > 3 \times 10^{-15} \text{ erg cm}^{-2} \text{ s}^{-1}$) as a function of radius, in units of r_{500} . A total of 3055 sources were included in the calculation of this profile. (c): The surface density of X-ray bright hard band sources ($F_X(2.0 - 8.0 \text{ keV}) > 10^{-14} \text{ erg cm}^{-2} \text{ s}^{-1}$) as a function of radius, in units of r_{500} . A total of 2933 sources were included in the calculation of this profile.

5.0.2 The XLF Model

Before presenting the results from our MCMC runs, it is important to discuss the choice of XLF for this study in more detail. For this study, we assume the Luminosity-Dependent Density Evolution (LDDE) XLF model of Ueda et al. (2014). The XLF of Ueda

et al. (2014) was determined in the rest frame 2–10 keV band, while we are using the 0.5–8.0 keV band in order to maximize the statistics of our measurement. In order to account for this energy band conversion, we convert the relevant parameters of the Ueda et al. (2014) model (L_* , L_{a1} & L_{a2}) to the full band assuming a power-law

photon index of $\Gamma = 1.4$. Additionally, we allow our priors to have statistical uncertainties a factor of 2 larger than the error bars published in Ueda et al. (2014), in order to account for the fact that the XLF may take on slightly different shapes in these two energy bands. However, the majority of the parameters for this model of the XLF are consistent with those measured in softer energy bands (Hasinger et al. 2005), suggesting that this procedure should not introduce any significant systematic error in our analysis. We also emphasize that this model is almost identical to the model of Ueda et al. (2003) at the redshifts of the clusters.

This luminosity function takes a double power-law form, parameterized as:

$$\frac{d\Phi(L_X, 0)}{d \log L_X} = \frac{A_0}{[L_X/L^*]^{\gamma_1} + [L_X/L^*]^{\gamma_2}} \quad (6)$$

where $\frac{d\Phi(L_X, 0)}{d \log L_X}$ is the differential number density of X-ray AGN (in units of Mpc^{-3} per logarithmic unit of luminosity) at redshift $z = 0$. For the LDDE model we have chosen, redshift evolution in the luminosity function is parameterized as

$$\frac{d\Phi(L_X, z)}{d \log L_X} = \frac{d\Phi(L_X, 0)}{d \log L_X} e(z) \quad (7)$$

with a redshift correction factor $e(z)$ that takes the form of

$$e(z) = \begin{cases} (1+z)^{p_1} & : z \leq z_{c1} \\ (1+z_{c1})^{p_1} \left(\frac{1+z}{1+z_{c1}}\right)^{p_2} & : z_{c1} < z \leq z_{c2} \\ (1+z_{c1})^{p_1} \left(\frac{1+z}{1+z_{c1}}\right)^{p_2} \left(\frac{1+z}{1+z_{c2}}\right)^{p_3} & : z > z_{c2} \end{cases}$$

where z_{c1} & z_{c2} are the two transition redshifts between the different evolution indexes (p_1 , p_2 , & p_3). In the LDDE model, the transition redshifts also depend on luminosity as

$$z_{c1}(L_X) = \begin{cases} z_{c1}^* & : L_X > L_{a1} \\ z_{c1}^* \left(\frac{L_X}{L_{a1}}\right)^{\alpha_1} & : L_X < L_{a1} \end{cases}$$

and similarly for z_{c2}

$$z_{c2}(L_X) = \begin{cases} z_{c2}^* & : L_X > L_{a2} \\ z_{c2}^* \left(\frac{L_X}{L_{a2}}\right)^{\alpha_2} & : L_X < L_{a2} \end{cases}$$

Finally, the first evolution index p_1 scales with luminosity as

$$p_1(L_X) = p_1^* + \beta_1 \times (\log L_X - 44) \quad (8)$$

The full set of parameter values utilized for our study including their priors are found in Table 3.

6 RESULTS ON CLUSTER MASS AND REDSHIFT DEPENDENT PARAMETERS

We find most parameters in our model to be consistent with their respective null hypotheses. For example, there is no significant evidence in our data for the spatial distribution of AGN in galaxy clusters to vary in a statistically significant manner with either the cluster redshift or mass (i.e. β_z & β_m are consistent with 0). The scaling factor does not have any significant redshift dependence (i.e. $\eta \sim 0$). However, the scaling factor does appear to have a strong mass dependence (i.e. $N \sim M^\zeta$): the null hypothesis of $\zeta = 0$ can be rejected at high ($\gtrsim 99.9\%$) confidence. With all four parameters of interest (i.e. ζ , η , β_z , & β_m) free (hereafter Model 1), the mode (i.e. the peak of the posterior distribution) is located at approximately $\zeta \sim -1.6$, with a 68.3% confidence interval of $\sim [-2.1, -0.9]$. We have further confirmed the robustness of this result by comparing

the posterior distributions of two independent sub-samples of clusters, each of which gives consistent measurements for the posterior distributions of all four parameters. This result provides clear evidence for peculiar evolution of X-ray AGN in galaxy clusters beyond the expectations from the field. To explore this result further, we present the results of posterior probability distributions from three additional models, the results of which are shown in Figure 7: Model 2 fixes all of the cluster mass and redshift dependent terms to 0 with the exception of ζ ; Model 3 includes both ζ and β_m as free parameters; while Model 4 allows ζ and η to be free parameters. Model 2 provides the most precise constraints on the mass dependent evolution of the scaling factor. Model 3 demonstrates that the mass-dependent scaling factor we measure is not degenerate with a dependence in the spatial distribution of the cluster AGN. Model 4 shows that our sample of cluster AGN evolves with redshift in a manner consistent with expectations from the field, and also that we have the statistical power to distinguish between mass-dependent and redshift-dependent models. Other models that freeze and thaw different combinations of these four parameters have also been examined, and the results of those models are consistent with the four models presented in this text.

The 1-dimensional posterior probability distributions along with the priors are summarized in Table 4. In Table 4, we list the mode and the 68% confidence interval about that mode for each free parameter. The posterior probability distributions are typically non-Gaussian in shape, and often have long asymmetric tails extending beyond their modes. Our sample provides little to no constraint regarding the redshift dependence of the scaling factor (η). The data are also consistent with a redshift and mass-independent radial profile for the cluster X-ray AGN. Our most constraining model for a mass dependent scaling factor constrains the value of that power-law slope to $\zeta \in [-3.71, -0.60]$ for its 99% confidence interval.

6.1 Physical Interpretation

The most straightforward interpretation of the $M^{-1.2}$ scaling relation that we observe is that it is driven by galaxy mergers within the cluster. Using virial arguments, we expect that the galaxy velocity dispersion, σ , in clusters will scale with cluster mass as $\sim M^{1/3}$. Additionally, theoretical calculations suggest that the rate of mergers between cluster galaxies should scale as $\sim \sigma^{-3}$ (Mamon 1992), or equivalently $\sim M^{-1}$, consistent with the $M^{-1.2}$ scaling observed in these data (Model 2).

Other physical explanations beyond a merger-driven scenario may possibly result in the observed number density profiles for these data. Any alternative model, however, would have to provide consistent results for all four mass and redshift dependent parameters. The absence of any dependence in the spatial distribution of these AGN with cluster mass and redshift suggests that galaxy-ICM interactions such as ram pressure stripping are not responsible for driving this scaling relation: it is unlikely that these process would operate on the same length scales (in units of r_{500}) irrespective of mass yet lower the overall scaling factor so noticeably, especially since the physical length of r_{500} in each cluster scales with mass. Further simulation work of cluster galaxies falling through realistic ICM environments from large distances will be necessary to further investigate these possibilities, however.

Table 3. Input priors on the MCMC runs of our four models. Nearly all of these priors are determined by the measurements of the XLF after converting published results to our energy band. All of the priors with error bars shown are assumed to be normally distributed, while those without error bars are fixed. Our priors have error bars a factor of 2 larger than the published values in order to account for any potential systematics that may arise in the energy band conversion. The only additional prior included in our analysis is for C , the projected density of X-ray AGN in the field as determined by *COSMOS*, assumed to be normally distributed with a variance of 10%, which is sufficiently large to account for both the statistical fluctuations and cosmic variance in this measurement.

XLF Priors	
Parameter	Prior
A_0 (Mpc $^{-3}$ dex $^{-1}$)	$(2.91 \pm 0.14) \times 10^{-6}$
γ_1	0.96 ± 0.08
γ_2	2.71 ± 0.18
$\log L_\star$	43.97 ± 0.12
p_1^*	4.78 ± 0.16
p_2	-1.5
p_3	-6.2
z_{c1}^*	1.86 ± 0.14
z_{c2}^*	3.0
β_1	0.84 ± 0.36
$\log L_{a1}$	44.61 ± 0.14
$\log L_{a2}$	44.00
α_1	0.29 ± 0.04
α_2	-0.1
C (deg $^{-2}$)	330 ± 33

Table 4. The resulting parameter values from our posterior probability distributions for all four models. For each parameter, we show the mode and the 68% confidence interval about that value, as determined by the 1-dimensional posterior probability distributions. We find that only one parameter shows statistically significant deviations from our field prediction: ζ , the power-law dependence of the scaling factor with mass.

Posteriors				
Parameter	Model 1	Model 2	Model 3	Model 4
η	$1.90^{+2.2}_{-1.8}$	0	0	$0.97^{+3.03}_{-2.89}$
ζ	$-1.63^{+0.50}_{-0.75}$	$-1.18^{+0.30}_{-0.80}$	$-1.28^{+0.35}_{-0.45}$	$-1.32^{+0.34}_{-0.51}$
β_0	$-1.55^{+1.30}_{-2.00}$	$-0.63^{+0.18}_{-0.14}$	$-0.67^{+0.21}_{-0.16}$	-0.67 ± 0.14
β_z	$0.78^{+1.40}_{-1.00}$	0	0	0
β_m	$-0.18^{+0.35}_{-0.20}$	0	$-0.03^{+0.16}_{-0.28}$	0
C (deg $^{-2}$)	350^{+12}_{-12}	345^{+14}_{-20}	342^{+11}_{-17}	335^{+14}_{-18}

7 PRELIMINARY SPECTRAL IDENTIFICATION AND VISUAL CLASSIFICATION OF CLUSTER MEMBER AGN

We have carried out a preliminary attempt to confirm cluster member AGN spectroscopically by searching the NASA/IPAC Extragalactic Database (NED) for optical spectroscopic counterparts for our X-ray point source positions. The search circle around each X-ray source is $2''$, sufficiently large to account for the expected positional uncertainties on our X-ray sources. Control tests that added random offsets to the X-ray source positions suggest that our expected number of “false positives” (i.e. finding a spectroscopic counterpart at the cluster redshift by chance coincidence) is negligible. Where we find a spectroscopic counterpart to the X-ray source with a redshift z_{cp} satisfying $c|z_{cluster} - z_{cp}| < 5000 \text{ km s}^{-1}$, we identify that X-ray source to be a spectroscopically confirmed cluster member. In total, we find that 88 of our X-ray AGN have spectroscopic counterparts within $2''$ of the source position.

We then searched the *Hubble* archive for images at each of these source positions made with either the ACS or WFC3 cameras. The *Hubble* images were registered to the *Chandra* images and cleaned of cosmic rays using the Laplacian edge detection algorithm of van Dokkum (2001). After these steps, 23 of the X-ray AGN had *Hubble* images deemed suitable for a preliminary visual classification of their morphologies.

Source catalogs for each *Hubble* field were produced using SEXTRACTOR (Bertin & Arnouts 1996) in a single filter. For each X-ray AGN we selected three control galaxies with similar optical magnitudes and clustercentric distances to the X-ray AGN. We then produced postage stamp images of the $5''$ radius surrounding each galaxy in both the AGN and control sample, utilizing up to three filters of imaging data for each galaxy when available. The postage stamp *Hubble* images for all 23 X-ray AGN can be found in Figure 8. Information about the filters and source positions are given in Table 5.

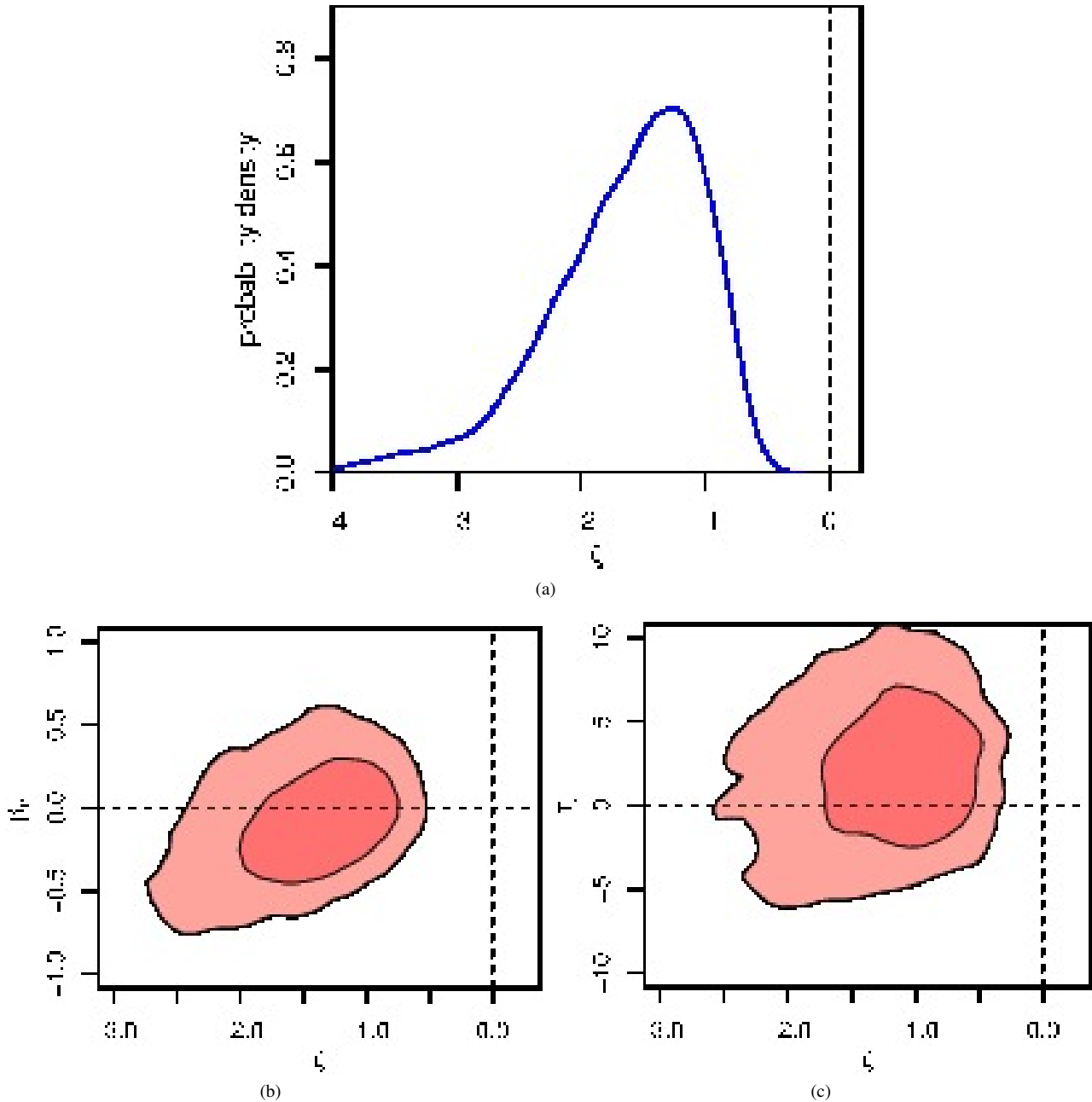


Figure 7. Posterior confidence intervals for model parameters. *Top:* The 1-dimensional posterior probability distribution for ζ in Model 2, where ζ is the only model parameter that is not fixed to its null value of 0. The null hypothesis of $\zeta = 0$ (denoted by the dashed vertical line) can be rejected at $> 99.9\%$ confidence. *Bottom Left:* The two-dimensional confidence contours (68.3% & 95.4%) for Model 2, where ζ and β_m are both free parameters. The null hypotheses of $\beta_m, \zeta = 0$ are denoted by the dashed lines. This model provides a consistent value for ζ as Model 2 and demonstrates that the mass dependence of Model 2 is inconsistent with arising from a mass-dependence in the spatial distribution of the cluster AGN. *Bottom Right:* The two-dimensional confidence contours (68.3% & 95.4%) for Model 3, where ζ and η are free parameters. The null hypotheses of $\eta, \zeta = 0$ are denoted by the dashed lines. This model provides a consistent value for ζ as Models 1 and 2 and demonstrates that the mass dependent scaling factor we observe is inconsistent with a model with a redshift dependence beyond the expected field evolution.

Galaxy morphologies were determined visually to fall into one of the following classes: 1) **Disturbed** galaxies which have clear signatures of disruptions from mergers such as tidal tails; 2) **Undisturbed** galaxies with no apparent disruptions; 3) Nearby **Neighbor** galaxies which, while not having evidence for major disruptions, are sufficiently near to other galaxies to suggest an imminent merger; 4) **Stellar** galaxies whose morphologies could not be distinguished from a point source; or 5) **Empty** images where the host

of the X-ray point source could not be determined. All of the co-authors except authors SE, RC, and AvdL did the morphology classification on all 92 galaxies. None of the participating co-authors knew which of the galaxies were the hosts of the X-ray AGN and which were control galaxies in advance. We then determined the fraction of galaxies within each of these morphological classes for both the normal galaxies and X-ray AGN.

Our main finding is that galaxies hosting X-ray AGN were

Table 5. Information about the *Hubble* images for all 23 spectroscopically confirmed X-ray AGN. For each source position, we denote the filters used for the images presented in Figure 8.

RA	DEC	Filter 1	Filter 2	Filter 3
3.53939	-30.41137	F606W		
3.55994	-30.37781	F606W		
3.61061	-30.39563	F606W		
4.63350	16.49064	F606W		
4.65420	16.46027	F775W	F606W	F555W
6.38361	-12.38467	F555W		
28.16550	-13.92369	F775W	F625W	
28.28761	-13.96692	CLEAR1L		
28.30403	-13.89717	F606W		
29.99430	-8.82704	F606W		
73.50511	2.96277	F606W		
73.55489	2.95945	F606W		
139.43829	51.71885	CLEAR1L		
146.80429	76.38735	F125W	F110W	F606W
151.72157	32.00314	F606W		
177.39105	22.37405	F775W	F606W	F475W
181.55492	-8.79565	F775W	F606W	F475W
186.71535	21.87390	F606W		
186.75880	33.56825	F775W	F625W	
212.63080	52.25929	F775W		
224.31136	22.32598	F850LP	F775W	
243.90677	-6.18664	F606W		
328.38098	17.69271	F125W	F850LP	

classified as **Disturbed** at higher rates than the control sample. The **Disturbed** vote fractions for the X-ray AGN and control sample are 22% (30/138) and 10% (43/414), respectively. We utilize a two-sided Student’s t-test to determine the probability of these two measurements arising from the same underlying population. Assuming a null hypothesis where the X-ray AGN and control samples have the same average fractions of disturbed galaxies, then we have a probability of $p = 0.043$ of measuring a larger absolute difference in the disturbed fractions of the two samples.⁷ Galaxies hosting X-ray AGN were equally likely to be classified as **Neighbor**, **Empty**, **Stellar**, and **Undisturbed** as their control galaxies. Applying a simple weighting scheme that weights more strongly sources where all voters agree on a particular classification leads to similar results. In conclusion, while there is some initial evidence that X-ray AGN in clusters may be preferentially hosted in galaxies with disturbed morphologies (consistent with a merger driven scenario), larger data samples and more robust (preferably automated) classification schemes will be required to further investigate the extent to which mergers may be responsible for the triggering of X-ray AGN in galaxy clusters.

One particular galaxy of note identified in this study is the X-ray AGN at RA(J2000) = 04^h54^m13.17^s, DEC(J2000) = +02°57^m34.0^s in the galaxy cluster Abell 520, a cluster galaxy which hosts a clear partial Einstein ring that has not yet been published in the literature.

⁷ This particular p value assumes equal variance for the X-ray AGN and control samples. If we don’t assume equal variance, then the probability of measuring a larger absolute difference in the means increases to $p = 0.097$.

8 DISCUSSION

A merger-driven scenario for the triggering of X-ray AGN in clusters would be interesting in the context of recent literature results. Investigations into the morphologies of X-ray AGN host galaxies in the field at similar X-ray luminosities, stellar masses, and redshifts to the sample presented here have found no connection between galaxy morphologies and the presence of an X-ray AGN (e.g. Gabor et al. 2009; Cisternas et al. 2011; Schawinski et al. 2011; Kocovski et al. 2012; Schawinski et al. 2012; Simmons et al. 2012; Fan et al. 2014). Our results therefore suggest that AGN in galaxy clusters may be triggered by distinct physical processes to those of field AGN. Further studies with larger samples of both cluster and field AGN will be necessary to understand the origins of this apparent dichotomy.

The $\sim M^{-1}$ scaling relation that we find may also play an important role in understanding the evolution of the AGN fraction in galaxy clusters over cosmic time. Previous work has demonstrated that the X-ray AGN fraction in this galaxy cluster sample is ~ 3 times lower than in the field (Paper II), while studies of lower mass (mean masses of $M_{500} \lesssim 10^{14}$), higher redshift clusters and groups ($z \sim 1$) appear to indicate higher fractions of AGN than in the field (Lehmer et al. 2013; Martini et al. 2013). The origin of the turnaround between these high redshift, low mass systems and lower redshift, more massive clusters may be driven by the fact that galaxy clusters grow continuously over cosmic time (and subsequently acquire higher velocity dispersions leading to lower merger rates).

Larger samples of galaxy clusters observed with *Chandra* and *Hubble* will be required to further investigate the origin of this signal, as all of the measurements here are limited by the sample statistics and not any systematic uncertainties in the XLF. Larger samples will be essential to place stronger constraints on the redshift dependent terms (η, β_z), as these terms in particular are not well constrained by these data. Recent Sunyaev-Zeldovich surveys of galaxy clusters such as those from the South Pole Telescope or Atacama Cosmology Telescope will be especially useful for similar studies as they offer more leverage for high redshift clusters than the studies utilized here. The morphological comparisons between cluster member X-ray AGN and control galaxies is also limited by the number statistics of spectroscopically confirmed X-ray AGN with both *Chandra* and *Hubble* imaging data.

From the theoretical side, more accurate calculations of the merger rate of galaxies in clusters will be required to further examine the scenario we propose. Our hypothesis that cluster AGN are driven by galaxy mergers hinges on the analytic prediction of the cluster galaxy merger rate in Mamon (1992), and we have not found literature results that discuss the accuracy of this prediction using N-body or hydrodynamic simulations of realistic galaxy clusters. Indeed, it remains uncertain whether the cluster galaxy merger rate scales with the cluster properties (such as redshift) or galaxy-specific properties (such as stellar mass or clustercentric distance) in ways unaccounted for in this analytic prediction. Confirming or refuting this prediction for the galaxy merger rate in clusters will provide critical information as to the interpretation of these results, and may also be able to provide other possible origins for the $\sim M^{-1.2}$ scaling relation we measure.

ACKNOWLEDGMENTS

We thank Patrick Broos and Leisa Townsley for technical support, insight, and advice as to how to utilize best the \AA software

package for this study. We also thank Bret Lehmer for providing the cumulative number counts data for the *CDFS* and Nina Bonaventura at the *Chandra* X-ray Center's Helpdesk for technical support in the catalog production. Support for this work was provided by the Department of Energy Grant Number DE-AC02-76SF00515 and *Chandra* X-ray Center grant GO0-11149X. Support for SE was provided by the Smithsonian Astrophysical Observatory (SAO) subcontract SV2-82023 under NASA contract NAS8-03060. We also acknowledge support from NASA ADP grant NNX10AC99G, *Chandra* X-ray Center grants SP1-12007A, and National Science Foundation grants AST-0838187 & AST-1140019. We also acknowledge support from the Thousand Young Talents (QingNianQianRen) program (KJ2030220004), the USTC startup funding (ZC9850290195), and the National Natural Science Foundation of China through NSFC-11243008. Additional funding as provided by the Strategic Priority Research Program "The Emergence of Cosmological Structures" of the Chinese Academy of Sciences (XDB09000000). This research has made use of the NASA/IPAC Extragalactic Database (NED) which is operated by the Jet Propulsion Laboratory, California Institute of Technology, under contract with the National Aeronautics and Space Administration. Based on observations made with the NASA/ESA Hubble Space Telescope, and obtained from the Hubble Legacy Archive, which is a collaboration between the Space Telescope Science Institute (STScI/NASA), the Space Telescope European Coordinating Facility (ST-ECF/ESA) and the Canadian Astronomy Data Centre (CADM/NRC/CSA).

REFERENCES

- Allen S. W., Evrard A. E., Mantz A. B., 2011, *ARA&A*, 49, 409
Applegate D. E., von der Linden A., Kelly P. L., Allen M. T., Allen S. W., Burchat P. R., Burke D. L., Ebeling H., Mantz A., Morris R. G., 2014, *MNRAS*, 439, 48
Bauer F. E., Alexander D. M., Brandt W. N., Schneider D. P., Treister E., Hornschemeier A. E., Garmire G. P., 2004, *AJ*, 128, 2048
Bertin E., Arnouts S., 1996, *Ap&SS*, 117, 393
Böhringer H., Schuecker P., Guzzo L., Collins C. A., Voges W., Cruddace R. G., Ortiz-Gil A., Chincarini G., De Grandi S., Edge A. C., MacGillivray H. T., Neumann D. M., Schindler S., Shaver P., 2004, *A&A*, 425, 367
Brandt W. N., Hasinger G., 2005, *ARA&A*, 43, 827
Broos P. S., Townsley L. K., Feigelson E. D., Getman K. V., Bauer F. E., Garmire G. P., 2010, *ApJ*, 714, 1582
Budzynski J. M., Kuposov S., McCarthy I. G., McGee S. L., Belokurov V., 2012, *ArXiv e-prints*
Burenin R. A., Vikhlinin A., Hornstrup A., Ebeling H., Quintana H., Mescheryakov A., 2007, *ApJS*, 172, 561
Cappelluti N., Allevato V., Finoguenov A., 2012, *Advances in Astronomy*, 2012
Cisternas M., Jahnke K., Inskip K. J., Kartaltepe J., Koekemoer A. M., Lisker T., Robaina A. R., Scodreggio M., Sheth K. e., 2011, *ApJ*, 726, 57
Cowie L. L., Garmire G. P., Bautz M. W., Barger A. J., Brandt W. N., Hornschemeier A. E., 2002, *ApJL*, 566, L5
Dressler A., 1980, *ApJ*, 236, 351
Ebeling H., Barrett E., Donovan D., Ma C.-J., Edge A. C., van Speybroeck L., 2007, *ApJL*, 661, L33

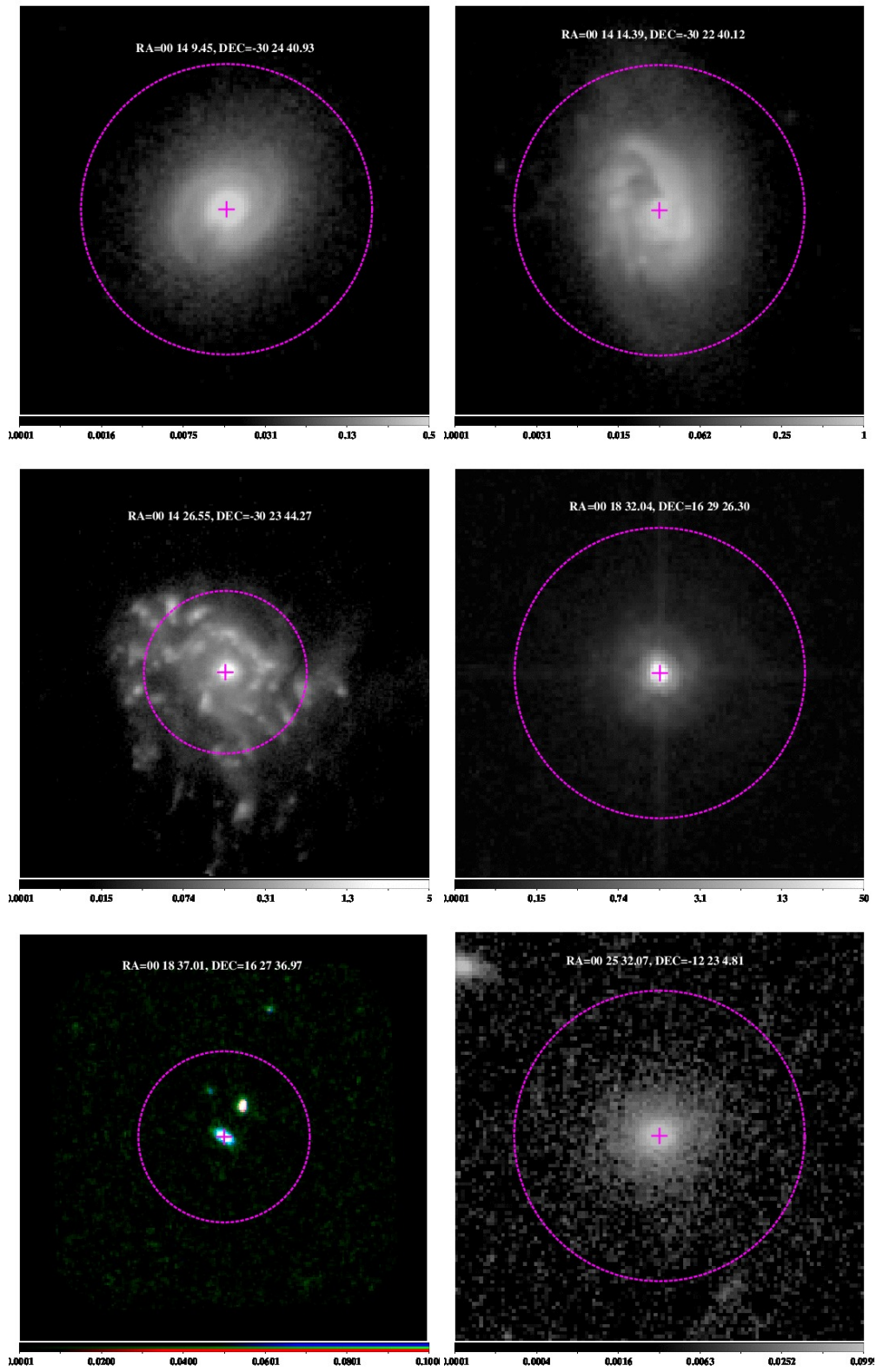


Figure 8. The 23 spectroscopically confirmed X-ray images in our sample with follow-up *Hubble* imaging. The cross in each image denotes the position of the X-ray source, and the dashed circle corresponds to a radius of $2''$ surrounding the AGN, which is roughly a factor of two larger than the positional uncertainty for all of our X-ray sources.

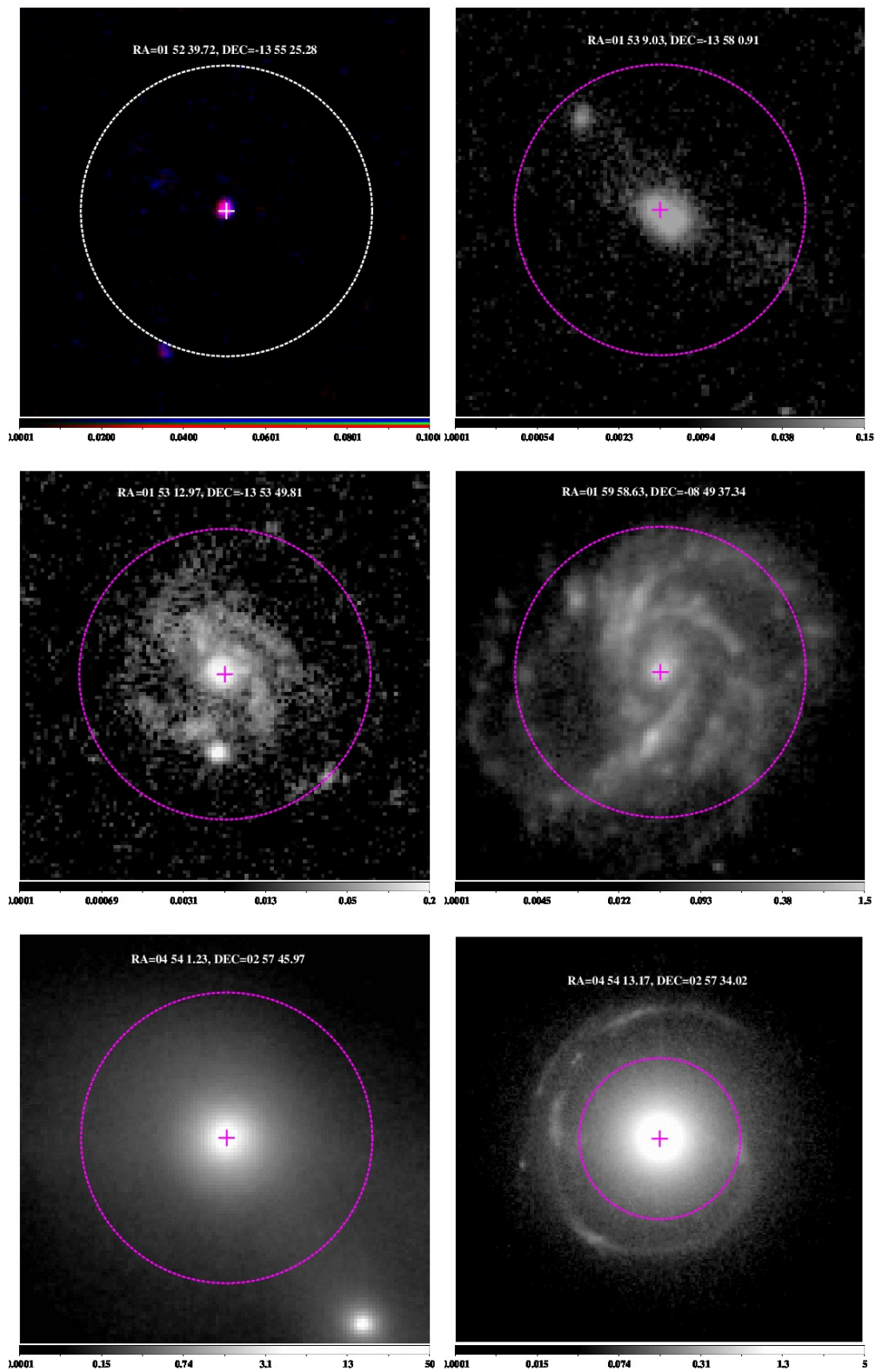
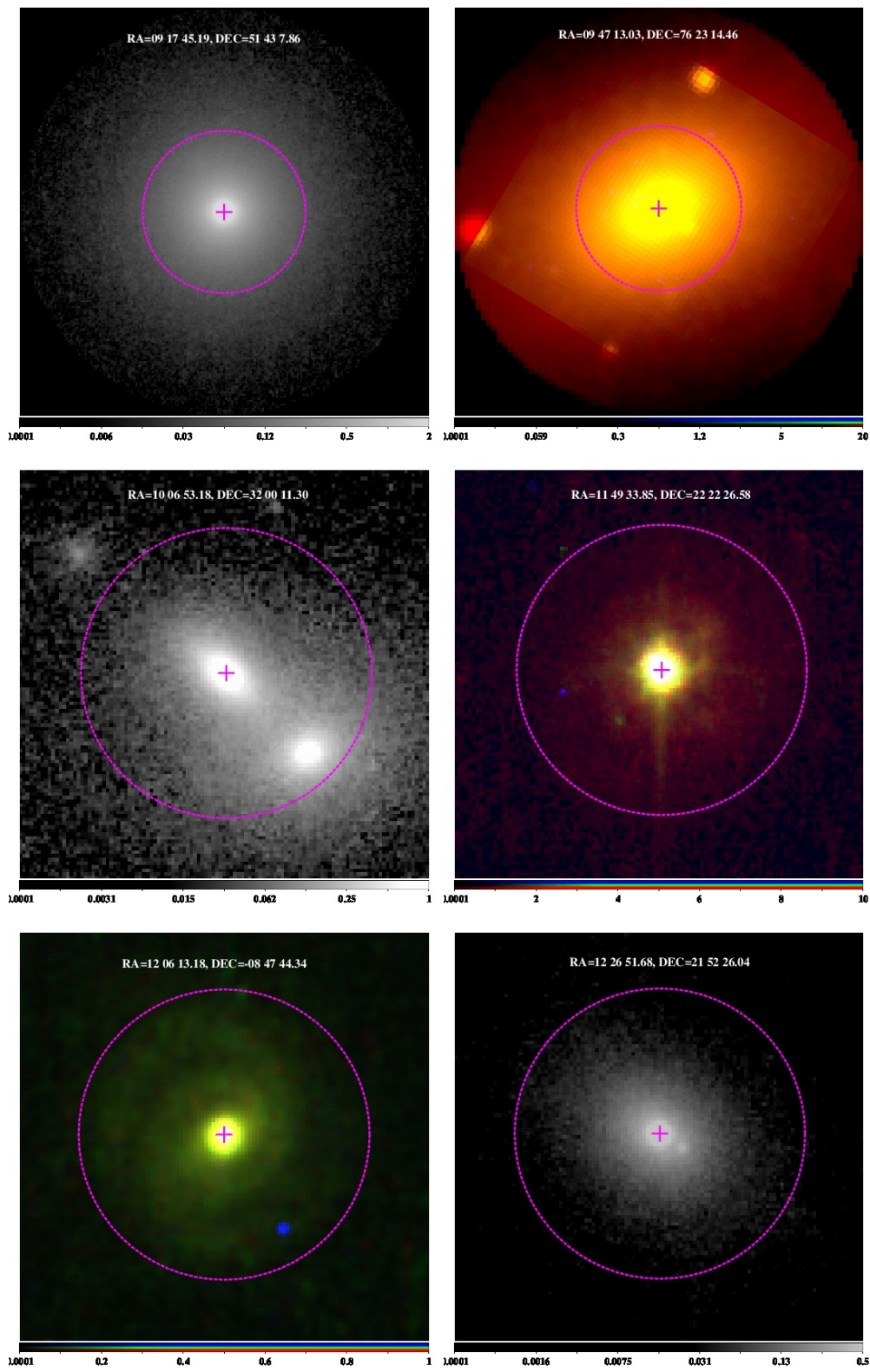


Figure 8. Continued. The bottom right image in this panel is a galaxy with a previously unpublished partial Einstein ring.



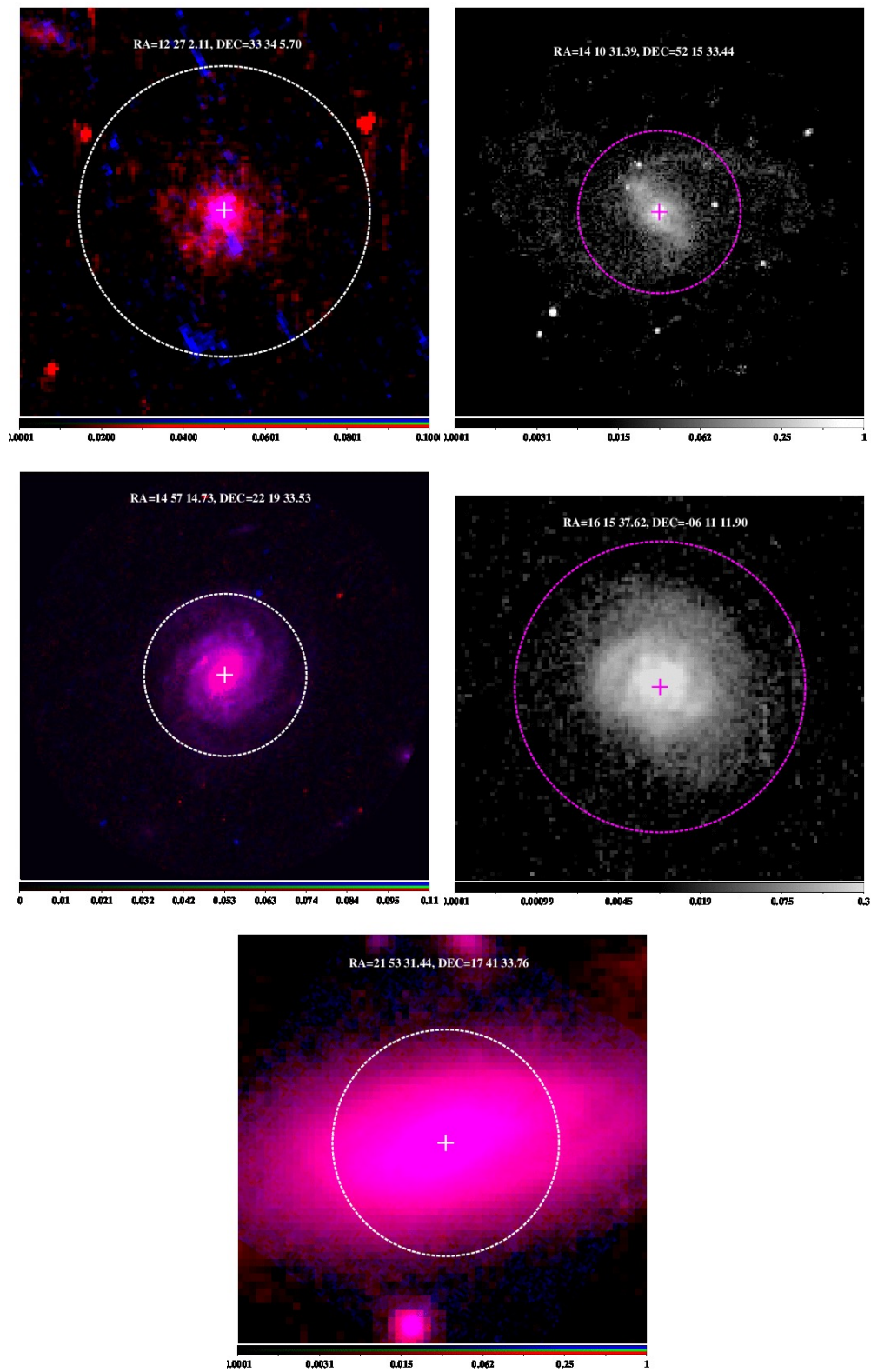


Figure 8. Continued

- Ebeling H., Edge A. C., Bohringer H., Allen S. W., Crawford C. S., Fabian A. C., Voges W., Huchra J. P., 1998, *MNRAS*, 301, 881
- Ebeling H., Edge A. C., Mantz A., Barrett E., Henry J. P., Ma C. J., van Speybroeck L., 2010, *MNRAS*, 407, 83
- Ehlert S., Allen S. W., Brandt W. N., Xue Y. Q., Luo B., von der Linden A., Mantz A., Morris R. G., 2013, *MNRAS*, 428, 3509
- Ehlert S., von der Linden A., Allen S. W., Brandt W. N., Xue Y. Q., Luo B., Mantz A., Morris R. G., Applegate D., Kelly P., 2014, *MNRAS*, 437, 1942
- Elvis M., Civano F., Vignali C., Puccetti S., Fiore F. e., 2009, *ApJS*, 184, 158
- Fan L., Fang G., Chen Y., Li J., Lv X., Kraiberg Knudsen K., Kong X., 2014, *ArXiv e-prints*
- Ferrarese L., Merritt D., 2000, *ApJL*, 539, L9
- Gabor J. M., Impey C. D., Jahnke K., Simmons B. D., Trump J. R., Koekemoer A. M., Brusa M., Cappelluti N., Schinnerer E., Smolčić V., Salvato M., Rhodes J. D., Mobasher B., Capak P., Massey R., Leauthaud A., Scoville N., 2009, *ApJ*, 691, 705
- Gehrels N., 1986, *ApJ*, 303, 336
- Georgakakis A., Coil A. L., Laird E. S., Griffith R. L., Nandra K., Lotz J. M., Pierce C. M., Cooper M. C., Newman J. A., Koekemoer A. M., 2009, *MNRAS*, 397, 623
- Gilmour R., Best P., Almaini O., 2009, *MNRAS*, 392, 1509
- Gunn J. E., Gott III J. R., 1972, *ApJ*, 176, 1
- Haggard D., Green P. J., Anderson S. F., Constantin A., Aldcroft T. L., Kim D.-W., Barkhouse W. A., 2010, *ApJ*, 723, 1447
- Hasinger G., 2008, *A&A*, 490, 905
- Hasinger G., Miyaji T., Schmidt M., 2005, *A&A*, 441, 417
- Hopkins A. M., Beacom J. F., 2006, *ApJ*, 651, 142
- Hopkins P. F., Hernquist L., Cox T. J., Kereš D., 2008, *ApJS*, 175, 356
- Kelly P. L., von der Linden A., Applegate D. E., Allen M. T., Allen S. W., Burchat P. R., Burke D. L., Ebeling H., Capak P., Czoske O., Donovan D., Mantz A., Morris R. G., 2014, *MNRAS*, 439, 28
- Kocevski D. D., Faber S. M., Mozena M., Koekemoer A. M., Nandra K., Rangel C., Laird E. S., Brusa M., Wuyts S., Trump J. R. e., 2012, *ApJ*, 744, 148
- Lehmer B. D., Lucy A. B., Alexander D. M., Best P. N., Geach J. E., Harrison C. M., Hornschemeier A. E., Matsuda Y., Mul-laney J. R., Smail I., Sobral D., Swinbank A. M., 2013, *ApJ*, 765, 87
- Lehmer B. D., Xue Y. Q., Brandt W. N., Alexander D. M., Bauer F. E., Brusa M., Comastri A., Gilli R., Hornschemeier A. E., Luo B., Paolillo M., Ptak A., Shemmer O., Schneider D. P., Tozzi P., Vignali C., 2012, *ApJ*, 752, 46
- Mamon G. A., 1992, *ApJL*, 401, L3
- Mantz A., Allen S. W., Ebeling H., Rapetti D., 2008, *MNRAS*, 387, 1179
- Mantz A., Allen S. W., Ebeling H., Rapetti D., Drlica-Wagner A., 2010, *MNRAS*, 406, 1773
- Mantz A., Allen S. W., Rapetti D., Ebeling H., 2010, *MNRAS*, 406, 1759
- Martini P., Miller E. D., Brodwin M., Stanford S. A., Gonzalez A. H., Bautz M., Hickox R. C., Stern D., Eisenhardt P. R., Galametz A., Norman D., Jannuzi B. T., Dey A., Murray S., Jones C., Brown M. J. I., 2013, *ApJ*, 768, 1
- Moore B., Lake G., Katz N., 1998, *ApJ*, 495, 139
- Moretti A., Campana S., Lazzati D., Tagliaferri G., 2003, *ApJ*, 588, 696
- Popesso P., Biviano A., Böhringer H., Romaniello M., 2007, *A&A*, 464, 451
- Puccetti S., Vignali C., Cappelluti N., Fiore F., Zamorani G., Aldcroft T. L., Elvis M. e., 2009, *ApJS*, 185, 586
- Refregier A., Loeb A., 1997, *ApJ*, 478, 476
- Reichard T. A., Heckman T. M., Rudnick G., Brinchmann J., Kauffmann G., Wild V., 2009, *ApJ*, 691, 1005
- Sarazin C. L., 1988, *X-ray emission from clusters of galaxies*. Cambridge Astrophysics Series, Cambridge: Cambridge University Press
- Schawinski K., Simmons B. D., Urry C. M., Treister E., Glikman E., 2012, *MNRAS*, 425, L61
- Schawinski K., Treister E., Urry C. M., Cardamone C. N., Simmons B., Yi S. K., 2011, *ApJL*, 727, L31
- Silk J., Rees M. J., 1998, *A&A*, 331, L1
- Simmons B. D., Urry C. M., Schawinski K., Cardamone C., Glikman E., 2012, *ApJ*, 761, 75
- Tal T., van Dokkum P. G., Nelan J., Bezanson R., 2009, *AJ*, 138, 1417
- Truemper J., 1993, *Science*, 260, 1769
- Ueda Y., Akiyama M., Hasinger G., Miyaji T., Watson M. G., 2014, *ArXiv e-prints*
- Ueda Y., Akiyama M., Ohta K., Miyaji T., 2003, *ApJ*, 598, 886
- van Dokkum P. G., 2001, *PASP*, 113, 1420
- Vikhlinin A., Kravtsov A. V., Burenin R. A., Ebeling H., Forman W. R., Hornstrup A., Jones C., Murray S. S., Nagai D., Quintana H., Voevodkin A., 2009, *ApJ*, 692, 1060
- von der Linden A., Allen M. T., Applegate D. E., Kelly P. L., Allen S. W., Ebeling H., Burchat P. R., Burke D. L., Donovan D., Morris R. G., Blandford R., Erben T., Mantz A., 2014, *MNRAS*, 439, 2
- Xue Y. Q., Brandt W. N., Luo B., Rafferty D. A., Alexander D. M., Bauer F. E., Lehmer B. D., Schneider D. P., Silverman J. D., 2010, *ApJ*, 720, 368
- Xue Y. Q., Luo B., Brandt W. N., Bauer F. E., Lehmer B. D., Broos P. S., Schneider D. P., Alexander D. M., Brusa M., Comastri A., Fabian A. C., Gilli R., Hasinger G., 2011, *ApJS*, 195, 10